Phenomenological models of two-particle correlation distributions on transverse momentum in relativistic heavy-ion collisions

R. L. Ray and A. Jentsch

Department of Physics, The University of Texas at Austin, Austin, Texas 78712, USA

Two-particle, pair-number correlation distributions on two-dimensional transverse momentum (p_{t1}, p_{t2}) constructed from the particle production in relativistic heavy-ion collisions allow access to dynamical processes in these systems beyond what can be studied with angular correlations alone. Only a few measurements of this type have been reported in the literature, and phenomenological models, which facilitate physical interpretation of the correlation structures, are nonexistent. Ongoing efforts at the Relativistic Heavy-Ion Collider (RHIC) will provide a significant volume of these correlation measurements in the future. In anticipation of these new data, two phenomenological models are developed which describe two-dimensional (2D) correlation distributions on transverse momentum. One model is based on a collision event-by-event fluctuating blast wave. The other is based on event-by-event fluctuations in fragmenting color-flux tubes and in jets. Both models are shown to be capable of accurately describing the measured single-particle p_t distributions for minimum-bias Au+Au collisions at $\sqrt{s_{NN}} = 200$ GeV. Both models are then applied to preliminary, charged-particle correlation measurements on 2D transverse momentum. The capabilities of the two models for describing the overall structure of these correlations, the stability of the fitting results with respect to collision centrality, and the resulting trends of the dynamical fluctuations are evaluated. In general, both phenomenological models are capable of qualitatively describing the major correlation structures on transverse momentum and can be used to establish the required magnitudes and centrality trends of the fluctuations. Both models will be useful for interpreting the forthcoming correlation data from the RHIC.

I. INTRODUCTION

Two-particle correlations constructed from the particles produced in high-energy, heavy-ion collisions are affected by partonic and hadronic dynamics throughout the spatiotemporal evolution of the hot, dense collision system. These dynamics include soft and hard interactions as predicted by quantum chromodynamics (QCD), fragmentation and hadronization [1–3], partonic and hadronic collective flow [4], plus others [5,6]. For symmetric, unpolarized collision systems (e.g., $p + p$, Au+Au, Pb+Pb) near midrapidity, two-particle correlations can be completely described using the four kinematic and angular variables p_{t1}, p_{t2} (transverse momentum), η_1-η_2 (relative pseudorapidity[1]), and ϕ_1-ϕ_2 (relative azimuthal angle) [7–9]. Correlation measurements on two-dimensional (2D) $(\eta_1$-η_2, ϕ_1-$\phi_2)$ angular space within 2D bins on transverse momentum space (p_{t1}, p_{t2}) [10] should, in principle, represent all the statistically accessible information. Unfortunately, the absolute normalization of 2D angular correlations is poorly determined due to the arbitrary multiplicity fluctuations arising from finite-width multiplicity bins [11,12].[2] Measurements to date of

four-dimensional (4D), two-particle correlations [13–16] are therefore incomplete.

In Ref. [17], it was shown that two-particle, pair-number correlation distributions on (p_{t1}, p_{t2}) can be derived from measures of nonstatistical mean-p_t fluctuations and that these correlations determine the average value (normalization) of the 2D angular correlations in each (p_{t1}, p_{t2}) bin, thus allowing the experimental determination of the 4D correlations to be completed. However, experimental and theoretical efforts in correlation studies have mainly involved angular correlations, while measurements and analysis of pair-number correlations on (p_{t1}, p_{t2}) have received much less attention. A few such measurements have been reported by the NA49 Collaboration [18,19], the CERES Collaboration [20], and the STAR Collaboration [7,21,22]. A much larger volume of preliminary (p_{t1}, p_{t2}) correlation measurements by the STAR Collaboration exists [13,14].

In addition to controlling the normalization of angular correlations, the measurement and analysis of (p_{t1}, p_{t2}) correlations allow access to independent dynamical information beyond what can be gleaned from angular correlations alone.

---

[1]Pseudorapidity is defined as $\eta = -\ln[\tan(\theta/2)]$, where θ is the polar scattering angle relative to the beam direction.

[2]A derivation of normalized 2D angular correlations of binned total p_t, using an angular scale-dependent mean-p_t fluctuation method, is

given in Refs. [11,12]. Application of this method to normalize the pair-number angular correlations is problematic because the finite multiplicity bin-width contributes directly to eventwise multiplicity fluctuations in the angular bins.

For example, in the hydrodynamic picture, eventwise fluctuations in global temperature would not be manifest in angular correlations, but would produce a distinctive "saddle-shape" correlation on (p_{t1}, p_{t2}) [19,22]. In fragmentation-based models with jets, e.g., HIJING [23], where eventwise fluctuations occur in the angular positions and energies of the jets, analysis of angular correlations can determine the average number of jet-related pairs of particles per event. Analysis of (p_{t1}, p_{t2}) correlations can determine the variance of the fluctuating number of jet-related pairs, an independent quantity. Pair-number correlations on (p_{t1}, p_{t2}) in jet production models are sensitive to eventwise dynamical fluctuations in both the number and energy of the jets, thus providing access to additional dynamical information beyond that which can be studied with angular correlations.

Of equal importance is the close connection between number correlations on (p_{t1}, p_{t2}) and model-dependent interpretation of single-particle p_t spectrum data. In conventional hydrodynamic or blast-wave models [24], p_t spectrum data are analyzed with the intent of determining physical properties of the heavy-ion collision produced medium, or quark-gluon plasma (QGP). These properties include temperature, chemical potentials, and radial flow. Often, such models do not include eventwise fluctuations. They cannot produce correlations on (p_{t1}, p_{t2}) and are therefore unphysical. The absence of fluctuations affects the shape of the p_t spectrum and therefore the fits to the data, resulting in inaccurate measures of medium properties.

In high-energy minimum-bias $p + p$ collisions, a straightforward correspondence exists between angular and (p_{t1}, p_{t2}) correlation structures for unidentified charged particles as shown in Ref. [25]. Two correlation peaks appear on (p_{t1}, p_{t2}) at lower and higher p_t. Selecting pairs in the lower p_t peak results in angular correlations consistent with longitudinal fragmentation and charge ordering [26] as described by the LUND color-flux tube or color-string model [1]. Selecting the higher p_t pairs results in jet- and dijet-like angular correlations which are well described by PYTHIA [2].

For more complex nucleus + nucleus collision systems, interpreting the correlation structures on transverse momentum coordinates is less clear, as is understanding the correspondences between correlation structures in the two, respective subspaces. For example, in 2D angular correlations [27,28], an azimuthal quadrupole is readily apparent, which is interpreted as pressure-driven elliptic flow in the hydrodynamic picture. Peaked correlations at relatively small opening angles are usually interpreted as jets. Back-to-back correlations in relative azimuth are interpreted as dijets or other momentum-conserving processes. On the other hand, the correlation structures which have been observed so far on (p_{t1}, p_{t2}), a saddle shape [22] plus broad peak from about 1 to $2\,\mathrm{GeV}/c$ [13,14], are not so readily interpreted. Different dynamical mechanisms, for example, fluctuating jets and fragmentation versus fluctuating temperatures and radial flow, produce similar structures, as will be shown in this paper.

The purpose of the present work is to develop and test two phenomenological models of relativistic heavy-ion collisions, based on distinctly different dynamical frameworks, which can be used to interpret the correlation structures and

provide an efficient means for determining the nature and strength of the fluctuations, within each framework, which are required to describe the data. The required magnitudes and centrality trends of the various fluctuations within each model can be compared to that allowed by the corresponding theories, thereby testing the applicability of each theoretical framework. The phenomenologies presented here may help tease apart the underlying dynamical mechanisms and help guide theoretical developments.

The first model is based on a fluctuating blast wave (BW) [29,30]. The second is based on fluctuating, two-component fragmentation (TCF) motivated by the success of the Kharzeev and Nardi (KN) [31] "soft plus hard" two-component interaction model. The general efficacy and stability of the models are tested by fitting mathematical representations of preliminary correlation data for Au+Au collisions at $\sqrt{s_{NN}} = 200\,\mathrm{GeV}$ from the STAR Collaboration [13,14]. Trends in the centrality dependences of the several fluctuating quantities in the models are presented and discussed.

This paper is organized as follows. The general method for introducing dynamical fluctuations into the single- and two-particle momentum distributions is presented in Sec. II. Applications of this method for the BW and TCF models are derived in Secs. III and IV, respectively, where they are tested with respect to charged-particle p_t spectra data for Au+Au collisions at $\sqrt{s_{NN}} = 200\,\mathrm{GeV}$. In Sec. V, both models are further tested by fitting (p_{t1}, p_{t2}) correlation pseudodata. The efficacy of each model, as well as the stability and centrality trends of the fluctuating quantities are also discussed in Sec. V. A summary and conclusions are given in Sec. VI.

II. GENERAL FLUCTUATION MODEL

Single-particle distributions on binned coordinates are constructed by counting all particles within a given acceptance in all collision events within a centrality class. Two-particle distributions are similarly constructed using all pairs of particles within the acceptance. If all particles in all events are emitted from equilibrated sources having the same uniform temperature T, using the simplest hydrodynamic picture for illustration, then the eventwise single-particle and two-particle distributions are simply the statistical samples of the same underlying *parent* distribution. In this case, there are no correlations. To generate correlations, the parent distributions must vary from event to event and/or within the source distribution of each event. An arbitrary ith particle is assumed to be emitted from a region of the source having a local temperature T_i. If the corresponding temperatures for an arbitrary pair of particles in an event, e.g., T_i and T_j, fluctuate independently such that the average pairwise fluctuations about the mean temperature $\bar{T}$ vanish, where $\langle (T_i - \bar{T})(T_j - \bar{T}) \rangle_{i \neq j} = 0$, then the correlations will again vanish. Mean temperature $\bar{T}$ is the average emitting temperature for all particles in the event sample. Within this model, nonvanishing correlations can only occur when $\langle (T_i - \bar{T})(T_j - \bar{T}) \rangle_{i \neq j} \neq 0$.

For the present application, each phenomenological model includes two independent sources of fluctuations in the parent distributions, either (1) temperature and transverse flow velocity or (2) longitudinal color-flux tube energy, and jet number

and energy. In this section, parameters P and Q are used to represent these two parameter values.

We start with a binned, single-particle density distribution on transverse momentum corresponding to an arbitrary collision event j, given by $\rho_{j,p_t} \equiv n_{j,p_t}/\delta_{p_t}$, where n_{j,p_t} is the number of particles from the jth event in the transverse momentum bin at p_t (subscript p_t is the bin index) and δ_{p_t} is the width of the bin. We then construct the event average for the total number of events ϵ in a centrality class, given by

$$\bar{\rho}_{p_t} = \frac{1}{\epsilon} \sum_{j=1}^{\epsilon} \rho_{j,p_t} = \frac{1}{\epsilon} \sum_{j=1}^{\epsilon} \sum_{i=1}^{n_j} \kappa_{i:p_t}/\delta_{p_t}, \qquad (1)$$

where n_j is the number of particles in event j and $\kappa_{i:p_t}=1$ if the ith particle is emitted into the bin at p_t, and is zero otherwise. Throughout this paper, overlines denote event averages or other mean values.

For the phenomenological models considered here, we assume that the production mechanisms are characterized by quantities P, Q, etc., whose values may vary within each event and from one event to the next as explained above. Each particle (i) in an event (j) is assumed to be produced from a region of the source characterized by discrete variables P_{ij}, Q_{ij}. The density distribution for event j generated by particles produced with discrete, source variables P' and Q' is given by

$$\rho_{jP'Q',p_t} = \frac{1}{\delta_{p_t}} \sum_{i=1}^{n_j} [\kappa_{i:p_t}]_{P_{ij}=P', Q_{ij}=Q'}, \qquad (2)$$

where $\kappa_{i:p_t} = 1$ if the source quantities for the ith particle equal P' and Q' and the particle is emitted into the bin at p_t; otherwise it is zero. The jth event distribution is therefore

$$\rho_{j,p_t} = \sum_{P',Q'} \rho_{jP'Q',p_t} \qquad (3)$$

and the event-averaged, binned distribution is given by

$$\bar{\rho}_{p_t} = \frac{1}{\epsilon} \sum_{j=1}^{\epsilon} \sum_{P',Q'} \rho_{jP'Q',p_t} = \sum_{P',Q'} \frac{1}{\epsilon} \sum_{j=1}^{\epsilon} \rho_{jP'Q',p_t}. \qquad (4)$$

The present implementation of the phenomenological models is in terms of the probability distributions for particle emission from source regions having arbitrary values P' and Q'. These distributions are introduced in Eq. (4) using a series of particle sums given by (dropping the primes)

$$N_{PQ} \equiv \sum_{p_t} \sum_{j=1}^{\epsilon} \rho_{jPQ,p_t} \delta_{p_t}, \qquad (5)$$

$$N_P \equiv \sum_Q N_{PQ}, \qquad (6)$$

$$N \equiv \sum_P N_P, \qquad (7)$$

from which Eq. (4) becomes

$$\bar{\rho}_{p_t} = \sum_{P,Q} \frac{N}{\epsilon} \frac{N_P}{N} \frac{N_{PQ}}{N_P} \frac{1}{N_{PQ}} \sum_{j=1}^{\epsilon} \rho_{jPQ,p_t}. \qquad (8)$$

In Eq. (7), N is the total number of accepted particles produced in all collisions in the centrality class and $N/\epsilon \equiv \bar{N}$ is the mean multiplicity per event. Ratio N_P/N is the fraction of all particles emitted from sources with fluctuating parameter value P. Ratio N_{PQ}/N_P is the fraction of all particles emitted from source regions with parameter value P in which the other fluctuating emission quantity has value Q. For the models considered here, we assume that the source emission parameters P and Q fluctuate independently of each other, which allows the simplifying approximation $N_{PQ}/N_P \approx N_Q/N$. The last ratio in Eq. (8) defines a unit-normal, binned distribution where

$$\hat{\rho}_{PQ,p_t} \equiv \frac{1}{N_{PQ}} \sum_{j=1}^{\epsilon} \rho_{jPQ,p_t} \qquad (9)$$

and $\sum_{p_t} \delta_{p_t} \hat{\rho}_{PQ,p_t} = 1$. Throughout this paper, the "hat" symbol denotes a unit-normalized distribution.

In the BW and TCF models, the source emission parameters and the outgoing particle momentum are represented with continuous variables. The continuum limits of the above binned quantities are given by the following:

$$\bar{\rho}_{p_t} \to \bar{\rho}(p_t), \quad N_P/N \to dP f(P),$$
$$N_Q/N \to dQ g(Q), \quad \hat{\rho}_{PQ,p_t} \to \hat{\rho}(P,Q,p_t),$$

where $\int dp_t \hat{\rho}(P,Q,p_t) = 1$. The single-particle density is given by

$$\bar{\rho}(p_t) = \bar{N} \iint dP dQ f(P) g(Q) \hat{\rho}(P,Q,p_t). \qquad (10)$$

Similarly, the two-particle binned distribution[3] for particles labeled 1 and 2 is given by

$$\bar{\rho}_{p_{t1},p_{t2}} = \frac{1}{\epsilon} \sum_{j=1}^{\epsilon} \frac{\bar{N}}{n_j} \frac{n_j-1}{n_j} \sum_{P_1,Q_1} \sum_{P_2,Q_2} \rho_{jP_1Q_1,p_{t1}} \rho_{jP_2Q_2,p_{t2}}$$

$$= \frac{\bar{N}-1}{\bar{N}} \sum_{P_1,Q_1} \sum_{P_2,Q_2} \frac{1}{\epsilon} \sum_{j=1}^{\epsilon} \rho_{jP_1Q_1,p_{t1}} \rho_{jP_2Q_2,p_{t2}}, \qquad (11)$$

where factor $(n_j - 1)/n_j$ normalizes each event to the correct number of pairs of particles, counting both permutations, factor $\bar{N}/n_j$ eliminates statistical bias caused by multiplicity variations within the centrality bin using the $\Delta\sigma^2_{p_t:n}$ mean-p_t fluctuation quantity derived in Ref. [17], and in the second line the ensemble of events is restricted to have fixed multiplicity $\bar{N}$. In Eq. (11), particle 1 is assumed to be emitted from a region of the source where the production quantities have the values P_1 and Q_1, and similarly for particle 2. Introducing pair ratios, analogous to those in Eqs. (5)–(7), gives

$$N_{P_1Q_1P_2Q_2} \equiv \sum_{p_{t1},p_{t2}} \sum_{j=1}^{\epsilon} \rho_{jP_1Q_1,p_{t1}} \rho_{jP_2Q_2,p_{t2}}$$
$$\times \delta_{p_{t1}} \delta_{p_{t2}}, \qquad (12)$$

———

[3]Throughout this paper, symbol ρ represents both single- and two-particle distributions. The number of particle labels distinguishes the usage.

$$N_{P_1 P_2} \equiv \sum_{Q_1, Q_2} N_{P_1 Q_1 P_2 Q_2}, \tag{13}$$

$$N_{(2)} \equiv \sum_{P_1, P_2} N_{P_1 P_2}, \tag{14}$$

where Eq. (11) becomes

$$\bar{\rho}_{p_{t1}, p_{t2}} = \frac{\bar{N} - 1}{\bar{N}} \sum_{P_1, P_2} \sum_{Q_1, Q_2} \frac{N_{(2)}}{\epsilon} \frac{N_{P_1 P_2}}{N_{(2)}} \frac{N_{P_1 Q_1 P_2 Q_2}}{N_{P_1 P_2}}$$
$$\times \frac{1}{N_{P_1 Q_1 P_2 Q_2}} \sum_{j=1}^{\epsilon} \rho_{j P_1 Q_1, p_{t1}} \rho_{j P_2 Q_2, p_{t2}}. \tag{15}$$

In Eq. (14), $N_{(2)} = \epsilon \bar{N}^2$ is the total number of pairs in the event ensemble, including self-pairs, when all events have fixed multiplicity. Assuming that fluctuation parameters P and Q are independent results in $N_{P_1 Q_1 P_2 Q_2}/N_{P_1 P_2} \approx N_{Q_1 Q_2}/N_{(2)}$. The last ratio in Eq. (15) factors into the product of unit-normalized single-particle density distributions $\hat{\rho}_{P_1 Q_1, p_{t1}} \hat{\rho}_{P_2 Q_2, p_{t2}}$. Clearly, if $N_{P_1 P_2} = N_{P_1} N_{P_2}$ and $N_{Q_1 Q_2} = N_{Q_1} N_{Q_2}$, then the two-particle density in Eq. (15) factors into a product of single-particle densities, resulting in no correlations.

In the continuum limit, $\bar{\rho}_{p_{t1}, p_{t2}} \to \bar{\rho}(p_{t1}, p_{t2})$, $N_{P_1 P_2}/N_{(2)} \to dP_1 dP_2 f(P_1, P_2)$, $N_{Q_1 Q_2}/N_{(2)} \to dQ_1 dQ_2 g(Q_1, Q_2)$, $\hat{\rho}_{P_1 Q_1, p_{t1}} \to \hat{\rho}(P_1, Q_1, p_{t1})$, and similarly for particle 2. The two-particle density in the continuum limit is therefore

$$\bar{\rho}(p_{t1}, p_{t2}) = \bar{N}(\bar{N} - 1) \iiiint dP_1 dP_2 dQ_1 dQ_2 f(P_1, P_2)$$
$$\times g(Q_1, Q_2) \hat{\rho}(P_1, Q_1, p_{t1}) \hat{\rho}(P_2, Q_2, p_{t2}). \tag{16}$$

In the following sections, explicit functional models are presented for the single-particle distributions and the emitting source parameter distributions.

III. BLAST-WAVE MODEL WITH FLUCTUATIONS

A. Single-particle distribution

The fluctuating blast-wave model is based on the invariant phase-space source emission distribution of Schnedermann, Sollfrank, and Heinz (SSH) [29] and as further developed by Tomášik *et al.* [30]. In this model, the invariant momentum distribution is calculated by integrating over the space-time coordinates of the source function $S(x, p)$, given by

$$E\frac{d^3 N}{dp^3} = \frac{d^2 N}{2\pi m_t dm_t dy} = \int dx^4 S(x, p)$$
$$= \int \tau d\tau \int d\eta_s \int r dr \int d\varphi S(x, p), \tag{17}$$

where x, p are four-vectors, E is the total energy of the particle, $m_t = \sqrt{p_t^2 + m_0^2}$ is the transverse mass, and m_0 is assumed to be the pion rest mass. Space-time coordinates τ, η_s, r, and φ are the proper time, source rapidity defined by $(1/2) \ln[(t + z)/(t - z)]$, transverse radius, and azimuthal angle, respectively. From Ref. [30], Eq. (17) can be expressed

at midrapidity ($y = 0$) as

$$E\frac{d^3 N}{dp^3} = \frac{\tau_0 m_t}{4\pi^2 \hbar^3} \int_0^\infty r dr G(r) e^{\beta \mu_0} I_0[\beta p_t \sinh \eta_t(r)]$$
$$\times \int_{-\infty}^\infty d\eta_s \cosh \eta_s H(\eta_s)$$
$$\times \exp[-\beta m_t \cosh \eta_t(r) \cosh \eta_s], \tag{18}$$

where τ_0 is the mean emission proper time, $\beta = 1/T$ is the inverse temperature, μ_0 is the chemical potential, I_0 is a modified Bessel function, $G(r)$ and $H(\eta_s)$ are the transverse and longitudinal-rapidity source distributions, and $\eta_t(r)$ is the transverse flow rapidity. The latter is defined in terms of the transverse flow velocity $v_t(r)$, where

$$\eta_t(r) = \frac{1}{2} \ln\left(\frac{1 + v_t(r)}{1 - v_t(r)}\right), \tag{19}$$

$v_t(r) = \tanh \eta_t(r)$, and the flow velocity profile is assumed to follow a power-law distribution given by [32]

$$v_t(r) = a_0 \varrho^{n_{\rm flow}}, \quad \varrho \equiv r/R_0, \tag{20}$$

where R_0 is the transverse radius parameter of the source.

In deriving Eq. (18), Bjorken boost-invariant expansion [30,33] was assumed, which is conventional in BW models, where longitudinal flow rapidity equals η_s. The source distribution was assumed to be uniform on azimuth, e.g., no $\cos(2\phi)$ dependence, because the final-state particle-pair yield in the present application is integrated over relative azimuth intervals of either π or 2π where such correlations average to zero. We also assumed the following in order to simplify the model, to focus on the dominant sources of fluctuations in the p_t distribution, and to simplify the numerical integrations: (1) the Maxwell-Boltzmann limit for the emission function, (2) a constant chemical potential $\mu(r) \approx \mu_0$, (3) a constant source distribution $G(r)$ from $r = 0$ to maximum radius R_0, and (4) the shape of source distribution $H(\eta_s)$ is taken from measured $dN_{\rm ch}/d\eta$ distributions. For the latter, $H(\eta_s)$ is taken to be symmetric about $\eta_s = 0$ for symmetric collision systems and is represented by a modified Woods-Saxon distribution given by

$$H(\eta_s) = H(|\eta_s|) = \mathcal{N}_s \frac{1 + w|\eta_s|^2}{1 + \exp[(|\eta_s| - \eta_{sr})/\eta_{st}]}, \tag{21}$$

where $\mathcal{N}_s$ is a normalization constant and parameters w, η_{sr} (source range), and η_{st} (source end-point thickness) were fitted to the $dN_{\rm ch}/d\eta$ distributions for minimum-bias Au+Au collisions at $\sqrt{s_{NN}} = 200$ GeV reported by the PHOBOS Collaboration [34]. Parameter values $w = 0.02$, $\eta_{sr} = 3.45$, and $\eta_{st} = 0.73$ approximately describe the shapes of these data at each measured centrality.

For applications to correlations on transverse momentum, it is beneficial to display results on transverse rapidity, given by $y_t = \ln[(p_t + m_t)/m_0]$ at midlongitudinal rapidity, where $p_t = m_0 \sinh(y_t)$. Plotting the correlations on transverse rapidity, rather than p_t, enhances the visual access to correlation structures at both lower and higher p_t. In addition, transverse rapidity is an additively boost-invariant coordinate which facilitates studies of transverse fragmentation, i.e., jets.

The single-particle distribution on y_t at $y = 0$ (longitudinal midrapidity) is given by

$$\frac{d^2N}{dy_t d\eta} = 2\pi p_t \frac{dp_t}{dy_t}\frac{dy}{d\eta}\left(\frac{d^2N}{2\pi m_t dm_t dy}\right)$$

$$= 2\pi p_t^2\left(\frac{d^2N}{2\pi m_t dm_t dy}\right), \quad (22)$$

where $m_t dm_t = p_t dp_t$ and $\eta = \lim_{m_0 \to 0} y$ is pseudorapidity. Jacobians dp_t/dy_t and $dy/d\eta$ equal m_t and p_t/m_t, respectively, at midrapidity. The quantity in parentheses in Eq. (22) is either taken from experiment or calculated in the blast-wave model.

A collection of collision events within a centrality bin can be expected to have fluctuating properties due to fluctuating initial conditions [35,36] and the stochastic nature of the system evolution from the initial impact to final kinetic decoupling. Within the context of the BW model, we would therefore expect the source geometry, freeze-out temperature, and transverse flow to fluctuate from event to event. Furthermore, due to nonuniform initial conditions, the temperature and flow fields within each collision environment might also vary relative to the smooth, analytic distribution assumed in Eq. (18). Fluctuations in τ_0, G, H, μ_0, β, and η_t are therefore possible.

To account for these fluctuations, we calculate the ensemble average of eventwise fluctuating BW distributions for unidentified, charged particles within midrapidity acceptance $\Delta\eta$ (e.g., $\Delta\eta = 2$ for the STAR Time Projection Chamber (TPC) tracking detector [37]). The measured and BW model charged-particle density distributions are related as follows,

$$\bar{\rho}_{ch}(y_t) = \Delta\eta\frac{d^2N_{ch,exp}}{dy_t d\eta}$$

$$= \Delta\eta\frac{1}{\epsilon}\sum_{j=1}^{\epsilon}\frac{d^2N_{BW,j}}{dy_t d\eta} + \delta\bar{\rho}(y_t)$$

$$\equiv \frac{1}{\epsilon}\sum_{j=1}^{\epsilon}\rho_{BW,j}(y_t) + \delta\bar{\rho}(y_t)$$

$$\equiv \bar{\rho}_{BW}(y_t) + \delta\bar{\rho}(y_t), \quad (23)$$

where the measured charged-particle distribution is introduced in the first line. In Eq. (23), the summation includes ϵ collision events within a centrality event class and $\delta\bar{\rho}(y_t)$ is the residual between the BW model and the spectrum data. Quantities $\bar{\rho}_{ch}(y_t)$ and $\bar{\rho}_{BW}(y_t)$ give the event-average number of charged-particles per y_t bin and are normalized to the measured number of charged particles produced within the acceptance, $y_t \in [y_{t_{min}}, y_{t_{max}}]$, $\Delta\eta$, and 2π in azimuth.

Event averaging over τ_0 and μ_0 do not affect the shape of the distribution $\bar{\rho}_{BW}(y_t)$, and calculations show that fluctuations in $G(r)$, or in radius R_0, and in $H(\eta_s)$ produce minor effects relative to those generated by fluctuations in β and $\eta_t(r)$. We therefore fix τ_0, μ_0, $G(r)$, and $H(\eta_s)$ and only allow β and $\eta_t(r)$ to fluctuate from event to event as well as within the source distribution of each collision. Flow fluctuations are introduced by allowing the transverse flow rapidity to fluctuate about its nominal value where in the following

calculations $\eta_t(r)$ in Eq. (19) is replaced with $\eta_{t0}\eta_t(r)$, where η_{t0} is a random variable sampled from a peaked distribution whose variance is an adjustable parameter.

The BW distribution in Eq. (23), with fluctuating temperature and transverse flow, is given by

$$\bar{\rho}_{BW}(y_t) = \bar{N}\int d\beta f(\beta, \bar{\beta}, q_\beta)$$

$$\times \int d\eta_{t0} g(\eta_{t0}, \bar{\eta}_{t0}, \sigma_{\eta_t})\hat{\rho}(\beta, \eta_{t0}, y_t) \quad (24)$$

using the steps in Sec. II, where fluctuations in inverse temperature and transverse flow rapidity sample the probability densities $f(\beta, \bar{\beta}, q_\beta)$ and $g(\eta_{t0}, \bar{\eta}_{t0}, \sigma_{\eta_t})$, respectively. Both are assumed to be peaked distributions whose mean and variances are determined by parameters $\bar{\beta}$, q_β, $\bar{\eta}_{t0}$, and σ_{η_t}.

In applying the blast-wave model with fluctuating β and η_{t0}, it was assumed that the regions of the source where β and η_{t0} are greater than or smaller than the respective means are uniformly and randomly distributed. With this assumption, the summations in Eq. (8), for arbitrary values of β and η_{t0}, uniformly sample the entire source volume such that the resulting invariant momentum distribution is given by Eq. (18) when calculated with those specific β and η_{t0} values. Calculations of the emitted particle p_t spectrum from sources with either correlated β and η_{t0} fluctuations or with position correlated β, η_{t0} fluctuations require microscopic models or Monte Carlo simulations, e.g., EPOS [35] and NEXSPHERIO [38], both of which are well beyond the scope and intent of the present phenomenological study.

In Ref. [22], it was shown that the transverse momentum spectrum data from relativistic heavy-ion collisions can be accurately described for $p_t < 5\,\text{GeV}/c$ when the inverse temperature β of a Maxwell-Boltzmann (MB) distribution, $\exp[-\beta(m_t - m_0)]$, is convoluted with a γ distribution. The unit-normal γ distribution is given by

$$f_\gamma(\beta, \bar{\beta}, q_\beta) = \frac{q_\beta}{\bar{\beta}\Gamma(q_\beta)}\left(\frac{\beta q_\beta}{\bar{\beta}}\right)^{q_\beta - 1}e^{-\beta q_\beta/\bar{\beta}}, \quad (25)$$

where $\bar{\beta}$ is the mean and $1/q_\beta$ is the relative variance $\sigma_\beta^2/\bar{\beta}^2$. The above convolution integral gives [22]

$$\int_0^\infty d\beta f_\gamma(\beta, \bar{\beta}, q_\beta)e^{-\beta(m_t - m_0)}$$

$$= [1 + \bar{\beta}(m_t - m_0)/q_\beta]^{-q_\beta}, \quad (26)$$

a Levy distribution [39].

The transverse flow rapidity scale parameter was assumed to follow a similar peaked distribution except with a suppressed long-range tail which helps the numerical integrations converge. The distribution was chosen to be a modified Gaussian given by

$$g(\eta_{t0}, \bar{\eta}_{t0}, \sigma_{\eta_t}) = \mathcal{N}_g\eta_{t0}\exp\left[-\frac{1}{2}\left(\frac{\eta_{t0} - \bar{\eta}_{t0}}{\sigma_{\eta_t}}\right)^2\right], \quad (27)$$

where $\bar{\eta}_{t0} = 1$ (fixed) and $\mathcal{N}_g$ normalizes the distribution to unity over the domain $\eta_{t0} \in [0, \infty]$.
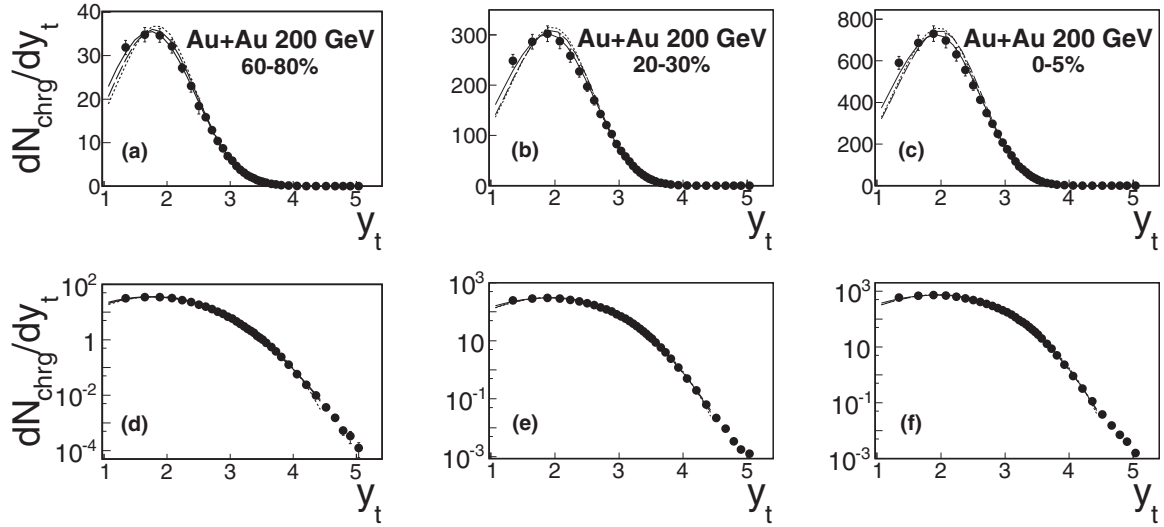
FIG. 1. Fluctuating blast-wave model fits to the 200 GeV Au+Au minimum-bias p_t spectrum data from STAR [40] showing only the 60–80%, 20–30%, and 0–5% centrality results. Yields are shown as quantity dN_{ch}/dy_t versus transverse rapidity y_t as defined in the text, assuming pseudorapidity acceptance $\Delta\eta = 2$. Linear (upper row) and semilog (lower row) plots are shown for the same data and curves to allow visual access to both lower and higher y_t fit results. Fit results assuming the full, nonflowing, and nonfluctuating BW models are shown by the solid, dashed, and dotted curves, respectively, as explained in the text.

The final form of the fluctuating blast-wave single-particle distribution is given by

$$\bar{\rho}_{BW}(y_t) = \bar{N} \int_0^\infty d\beta f_\gamma(\beta, \bar{\beta}, q_\beta)$$
$$\times \int_0^\infty d\eta_{t0} g(\eta_{t0}, \bar{\eta}_{t0}, \sigma_{\eta_t}) \hat{\rho}_{BW}(\beta, \eta_{t0}, y_t),$$
(28)

where

$$\hat{\rho}_{BW}(\beta, \eta_{t0}, y_t) = \mathcal{N} m_t p_t^2 \frac{\tau_0 R_0^2 G_0 \Delta\eta}{2\pi\hbar^3}$$
$$\times \int_0^1 \varrho d\varrho \, e^{\beta\mu_0} I_0[\beta p_t \sinh\eta_t(\varrho)]$$
$$\times \int_{-\infty}^\infty d\eta_s \cosh\eta_s H(\eta_s) e^{-\beta m_t \cosh\eta_t(\varrho)\cosh\eta_s}.$$
(29)

Constant $\mathcal{N}$ ensures that $\hat{\rho}_{BW}(\beta, \eta_{t0}, y_t)$ is normalized to unity in the domain $y_t \in [y_{t_{\min}}, y_{t_{\max}}]$. To compare with experiment, Eq. (29) was calculated at the y_t bin centers. In Eq. (29), the η_s integration was done numerically for discrete values of $\beta m_t \cosh\eta_t(\varrho)$ and saved for later interpolation during the three-dimensional (3D) numerical integration over variables β, η_{t0}, and ϱ. Integration limits and step sizes were studied to ensure sufficiently accurate convergence in the calculated y_t spectrum relative to the statistical errors in the data. The fit parameters in the single-particle BW model are $\bar{\beta}$ and q_β in Eq. (25), a_0 and n_{flow} in Eq. (20), and σ_{η_t} in Eq. (27), where $\bar{N}$ is taken from data. These fit parameters control the mean temperature and transverse flow profile plus the temperature and flow fluctuations.

The blast-wave model was applied to the charged particle p_t spectra data for Au+Au minimum-bias collisions at $\sqrt{s_{NN}} = 200$ GeV measured by the STAR Collaboration [40] for collision centralities 0–5%, 5–10%, 10–20%, 20–30%, 30–40%, 40–60%, and 60–80%. These data were fitted within the y_t range from 1.34 to 4.36, corresponding to p_t from 0.25 to 5.5 GeV/c. Three sets of fits were done in which (1) the full BW model was used where the five parameters above were freely varied, (2) a nonflowing ($a_0 = 0$), thermal fluctuation model was used, and (3) a nonfluctuating, pure BW model was used where $q_\beta = \sigma_{\eta_t} = 0$ while $\bar{\beta}$, a_0, and n_{flow} were freely varied. Best fits were based on minimum χ^2.

Quantitative descriptions of the data were obtained for all centralities using the full blast wave. Examples are shown in Fig. 1 for the 60–80%, 20–30%, and 0–5% centralities where fits produced by the full BW, the nonflowing thermal fluctuation BW, and the nonfluctuating BW are shown by the solid, dashed, and dotted curves, respectively. The BW model fit parameter values for all centralities and for each of the three model scenarios are listed in Table I. The residuals, $\delta\bar{\rho}(y_t)$ in Eq. (23), for the full BW model fits are of order 5% or less throughout the y_t and centrality ranges studied here.

The full BW model accurately describes the data over the entire y_t range considered in this analysis. The nonflowing, thermal fluctuation BW model overestimates the mode (peak position) but accurately describes the data at larger y_t. The nonfluctuating BW model overestimates the peak position by an even larger amount and underestimates the data at low y_t less than 1.5 and at the largest y_t bin considered here.

Typical, nonfluctuating blast-wave model fits to p_t spectrum data produce results where the temperature decreases and the average flow velocity increases with centrality [24]. In the present BW model application, the average flow velocity increases slightly with centrality, but the fitted temperature also increases. It should be noted that in the present

TABLE I. Blast-wave fit model parameters for the 200-GeV Au+Au minimum-bias p_t spectrum data from STAR [40] for the full BW model, the nonflowing BW, and the nonfluctuating BW as explained in the text. Data were fitted in the y_t range from 1.34 to 4.36 using 30 data points at each centrality. Temperature (T in GeV) equals $1/\beta$. Average transverse flow velocity $\bar{v}_t$ equals $2a_0/(n_{\text{flow}} + 2)$ in units where $c = 1$.

Centrality	Full BW							No flow BW			No fluct. BW				
(%)	T (GeV)	q_β	a_0	n_{flow}	σ_{η_t}	$\bar{v}_t$	$\frac{\chi^2}{\text{DoF}}$	T (GeV)	q_β	$\frac{\chi^2}{\text{DoF}}$	T (GeV)	a_0	n_{flow}	$\bar{v}_t$	$\frac{\chi^2}{\text{DoF}}$
0–5	0.110	20.2	0.68	0.49	0.051	0.55	2.10	0.172	16.1	2.38	0.184	0.76	5.8	0.20	6.54
5–10	0.112	19.8	0.66	0.47	0.065	0.53	1.92	0.169	15.6	2.23	0.180	0.76	5.0	0.22	5.45
10–20	0.110	18.7	0.68	0.57	0.033	0.53	1.34	0.166	14.8	2.04	0.180	0.77	5.2	0.21	4.00
20–30	0.105	17.5	0.70	0.60	0.018	0.54	1.01	0.162	14.1	1.66	0.186	0.78	7.0	0.17	4.12
30–40	0.103	16.7	0.70	0.64	0.043	0.53	1.26	0.157	13.5	1.85	0.172	0.80	5.5	0.21	4.72
40–60	0.100	15.3	0.47	0.04	0.38	0.46	0.64	0.144	12.2	1.15	0.172	0.82	7.5	0.17	3.00
60–80	0.082	12.9	0.75	0.89	0.02	0.52	0.56	0.129	11.1	1.08	0.162	0.84	8.2	0.16	3.13

application the fitting is performed over a larger p_t range than is usually addressed with blast-wave models [24] and the additional effects of fluctuations are included.

The results in Table I illustrate the risk associated with relying on nonfluctuating models to infer physical properties of the medium. The temperatures and transverse flow velocities inferred with the nonfluctuating BW model fits are approximately twice and one-half, respectively, the values inferred with the full, fluctuating BW model. At a minimum, eventwise fluctuating BW models, or event-by-event hydrodynamic models, e.g., EPOS [35] and NEXSPHERIO [38], should be used in such analyses. Ideally, both the spectrum and correlation data should be fit simultaneously.

B. Two-particle distribution

Two-particle distributions were calculated by summing over all pairs of particles from the same collision (same-event pairs denoted "se") for all events within a given centrality range. In the BW model, arbitrary pairs are emitted from two arbitrary regions of the source which are characterized by inverse temperature and transverse flow rapidity parameters (β_1, η_{t0_1}) and (β_2, η_{t0_2}), respectively. Correlations arise when the distributions of (β_1, η_{t0_1}) versus (β_2, η_{t0_2}) are correlated [22] (see Sec. II). Correlated fluctuations between β and η_{t0} are not considered here; only (β_1, β_2) and $(\eta_{t0_1}, \eta_{t0_2})$ correlated fluctuations are included in the present model, both for computational simplicity and in lieu of credible models of 4D $(\beta_1, \eta_{t0_1}, \beta_2, \eta_{t0_2})$ correlated fluctuations.

The two-particle, same-event BW density distribution, using Eqs. (11) and (23), is given by

$$\bar{\rho}_{\text{BW,se}}(y_{t1}, y_{t2}) = \frac{\bar{N} - 1}{\bar{N}} \frac{1}{\epsilon} \sum_{j=1}^{\epsilon} [\rho_{\text{BW},j}(y_{t1}) + \delta\bar{\rho}(y_{t1})]$$

$$\times [\rho_{\text{BW},j}(y_{t2}) + \delta\bar{\rho}(y_{t2})]$$

$$= \frac{\bar{N} - 1}{\bar{N}} \frac{1}{\epsilon} \sum_{j=1}^{\epsilon} [\rho_{\text{BW},j}(y_{t1})\rho_{\text{BW},j}(y_{t2})$$

$$+ \rho_{\text{BW},j}(y_{t1})\delta\bar{\rho}(y_{t2})$$

$$+ \rho_{\text{BW},j}(y_{t2})\delta\bar{\rho}(y_{t1}) + \delta\bar{\rho}(y_{t1})\delta\bar{\rho}(y_{t2})].$$

$$(30)$$

The event averages in the second and third terms are calculated as in the preceding subsection. The last term is simply $[(\bar{N} - 1)/\bar{N}]\delta\bar{\rho}(y_{t1})\delta\bar{\rho}(y_{t2})$. The first term can be expanded as in Sec. II and is given by

$$\bar{\rho}'_{\text{BW,se}}(y_{t1}, y_{t2})$$

$$\equiv \bar{N}(\bar{N} - 1) \int\int d\beta_1 d\beta_2 f(\beta_1, \beta_2)$$

$$\times \int\int d\eta_{t0_1} d\eta_{t0_2} g(\eta_{t0_1}, \eta_{t0_2})$$

$$\times \hat{\rho}_{\text{BW}}(\beta_1, \eta_{t0_1}, y_{t1})\hat{\rho}_{\text{BW}}(\beta_2, \eta_{t0_2}, y_{t2}). \quad (31)$$

In the absence of temperature correlations, $f(\beta_1, \beta_2)$ is simply a product of γ distributions for particles 1 and 2. This uncorrelated product of γ distributions can be expressed in terms of the sum and difference variables [22] $\beta_\Sigma = \beta_1 + \beta_2$ and $\beta_\Delta = \beta_1 - \beta_2$, and is given by

$$f_\gamma(\beta_1, \bar{\beta}, q_\beta)f_\gamma(\beta_2, \bar{\beta}, q_\beta) = f_\gamma(\beta_\Sigma, 2\bar{\beta}, 2q_\beta)\tilde{f}(\beta_\Sigma, \beta_\Delta, q_\beta),$$

$$(32)$$

where

$$\tilde{f}(\beta_\Sigma, \beta_\Delta, q_\beta) = \frac{\Gamma(2q_\beta)}{\Gamma(q_\beta)^2} \frac{1}{2^{2(q_\beta-1)}} \frac{1}{\beta_\Sigma} \left(1 - \frac{\beta_\Delta^2}{\beta_\Sigma^2}\right)^{q_\beta - 1} \quad (33)$$

and Γ is the Γ function. Parameters $\bar{\beta}$ and relative variance $\sigma_\beta^2/\bar{\beta}^2 = 1/q_\beta$ were determined by fitting the single-particle distributions (Table I).

When the source temperatures at arbitrary emission sites are correlated, the 2D distribution of β_1 and β_2 values for all particle pairs in the event collection has positive covariance as shown in the diagram in Fig. 2. Correlated temperature emission can be introduced in Eq. (33) by allowing the relative variances along the β_Σ and β_Δ directions to independently vary. We therefore define

$$f(\beta_1, \beta_2) \equiv f_\gamma(\beta_\Sigma, 2\bar{\beta}, 2q_{\beta_\Sigma})\tilde{f}(\beta_\Sigma, \beta_\Delta, q_{\beta_\Delta}). \quad (34)$$

The correlation data will be fitted by adjusting the relative variances along the β_Σ and β_Δ directions, $\sigma_{\beta_{\Sigma,\Delta}}^2/\bar{\beta}^2$, as shown in Fig. 2. The shifts in the relative variances are defined by parameters $\Delta(1/q)_\Sigma$ and $\Delta(1/q)_\Delta$, respectively, where

$$\Delta(1/q)_\Sigma = 1/q_{\beta_\Sigma} - 1/q_\beta,$$

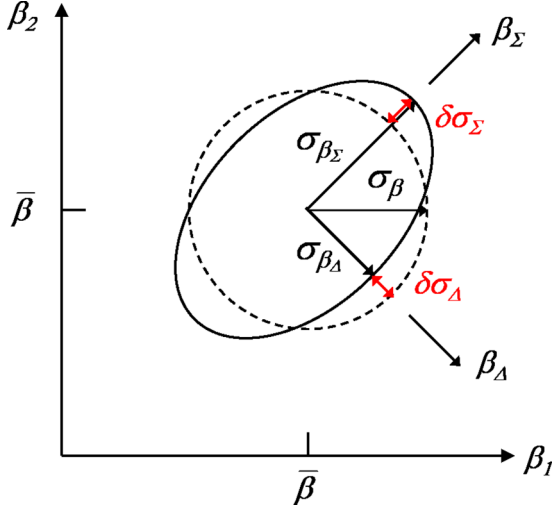$$\Delta(1/q)_\Delta = 1/q_{\beta_\Delta} - 1/q_\beta. \quad (35)$$

FIG. 2. Diagrammatic representation of a 2D scatter plot of the inverse temperatures (β_1 and β_2) for all pairs of particles (1,2) emitted from all events in a typical centrality bin. The dashed circle (solid ellipse) represents the 1-σ contour of an uncorrelated (correlated) distribution. The mean and 1σ width of the uncorrelated distribution are denoted by $\bar{\beta}$ and σ_β. Widths and changes in widths along the β_Σ and β_Δ directions for the correlated distribution are denoted by σ_{β_Σ}, $\delta\sigma_\Sigma$ and σ_{β_Δ}, $\delta\sigma_\Delta$, respectively.

If $\Delta(1/q)_\Sigma > \Delta(1/q)_\Delta$, then the β emissions are correlated and if $\Delta(1/q)_\Sigma < \Delta(1/q)_\Delta$, then they are anticorrelated. Results are more conveniently reported as the combinations

$$
\begin{aligned}
\Delta(1/q)_{\text{Vol}} &\equiv [\Delta(1/q)_\Sigma + \Delta(1/q)_\Delta]/2 \\
&= \frac{(\sigma_{\beta_\Sigma}^2 - \sigma_\beta^2)}{2\bar{\beta}^2} + \frac{(\sigma_{\beta_\Delta}^2 - \sigma_\beta^2)}{2\bar{\beta}^2}, \\
\Delta(1/q)_{\text{cov}} &\equiv [\Delta(1/q)_\Sigma - \Delta(1/q)_\Delta]/2 \\
&= \frac{\sigma_{\beta_\Sigma}^2 - \sigma_{\beta_\Delta}^2}{2\bar{\beta}^2},
\end{aligned} \tag{36}
$$

where $\Delta(1/q)_{\text{Vol}}$ measures the overall (volume) change in width of the 2D (β_1, β_2) distribution and $\Delta(1/q)_{\text{cov}}$ indicates the covariance.

Similarly, the transverse flow rapidity scale parameter 2D distribution can be written as a product of the single-particle distributions $g(\eta_{t0}, \bar{\eta}_{t0}, \sigma_{\eta_t})$. The product can be expressed in terms of sum and difference variables $\eta_{t0_{\Sigma,\Delta}} = \eta_{t0_1} \pm \eta_{t0_2}$, and the variances along η_{t0_Σ} and η_{t0_Δ} can be varied in order to fit the correlation data. The resulting correlated, transverse-flow rapidity scale parameter distribution is given by

$$
\begin{aligned}
g(\eta_{t0_1}, \eta_{t0_2}) &\equiv g_2\big(\eta_{t0_1}, \eta_{t0_2}, \bar{\eta}_{t0}, \sigma_{\eta_{t\Sigma}}, \sigma_{\eta_{t\Delta}}\big) \\
&= \mathcal{N}_{g_2} \eta_{t0_1} \eta_{t0_2} \exp\Bigg\{ -\frac{1}{2}\Bigg[\left(\frac{\eta_{t0_\Sigma} - 2\bar{\eta}_{t0}}{\sqrt{2}\sigma_{\eta_{t\Sigma}}}\right)^2 \\
&\quad + \left(\frac{\eta_{t0_\Delta}}{\sqrt{2}\sigma_{\eta_{t\Delta}}}\right)^2 \Bigg] \Bigg\},
\end{aligned} \tag{37}
$$

where $\mathcal{N}_{g_2}$ normalizes the 2D distribution to unity, the widths are defined as $\sigma_{\eta_{t\Sigma}} \equiv \sigma_{\eta_t} + \Delta_{\eta_t}/2$ and $\sigma_{\eta_{t\Delta}} \equiv \sigma_{\eta_t} - \Delta_{\eta_t}/2$, $\bar{\eta}_{t0}$ is fixed to 1, and parameter σ_{η_t} was determined by fitting the single-particle distributions (Table I).

Using Eqs. (29), (34), and (37) in Eq. (31) gives the 4D integration result

$$
\begin{aligned}
\bar{\rho}'_{\text{BW,se}}(y_{t1}, y_{t2}) &= \bar{N}(\bar{N} - 1) \iint d\beta_1 d\beta_2 f_\gamma\big(\beta_\Sigma, 2\bar{\beta}, 2q_{\beta_\Sigma}\big) \\
&\quad \times \tilde{f}(\beta_\Sigma, \beta_\Delta, q_{\beta_\Delta}) \iint d\eta_{t0_1} d\eta_{t0_2} \\
&\quad \times g_2\big(\eta_{t0_1}, \eta_{t0_2}, \bar{\eta}_{t0}, \sigma_{\eta_{t\Sigma}}, \sigma_{\eta_{t\Delta}}\big) \\
&\quad \times \hat{\rho}_{\text{BW}}\big(\beta_1, \eta_{t0_1}, y_{t1}\big) \hat{\rho}_{\text{BW}}\big(\beta_2, \eta_{t0_2}, y_{t2}\big).
\end{aligned} \tag{38}
$$

The same numerical integration ranges and step sizes used for the single-particle BW calculation were used in the numerical integration in Eq. (38).

C. Two-particle correlation

By definition, the two-particle correlations contained in the two-particle, BW distribution in Eq. (38) equal the difference between it and the product of marginals, where

$$
\bar{\rho}_{\text{BW,marg}}(y_{t1}) \equiv \frac{1}{\bar{N} - 1} \int dy_{t2} \bar{\rho}'_{\text{BW,se}}(y_{t1}, y_{t2}) \tag{39}
$$

with normalization $\int dy_{t1} \bar{\rho}_{\text{BW,marg}}(y_{t1}) = \bar{N}$. To ensure consistency with the single-particle measurements, we also require the marginal of the entire two-particle distribution in Eq. (30) to equal the measured charge distribution $\bar{\rho}_{\text{ch}}(y_t)$ in Eq. (23). However, in order to fit the correlation data, the variances in the inverse temperature and transverse flow rapidity, $\Delta(1/q)_{\text{Vol,cov}}$ and Δ_{η_t}, were freely varied, resulting in marginals which may not precisely equal $\bar{\rho}_{\text{BW}}(y_t)$ in Eq. (23). This condition requires an adjusted residual $\delta\bar{\rho}'(y_t)$ defined by

$$
\delta\bar{\rho}'(y_t) \equiv \bar{\rho}_{\text{ch}}(y_t) - \bar{\rho}_{\text{BW,marg}}(y_t). \tag{40}
$$

The adjusted residual is normalized such that $\int dy_t \delta\bar{\rho}'(y_t) = 0$ because both $\bar{\rho}_{\text{ch}}$ and $\bar{\rho}_{\text{BW,marg}}$ are normalized to $\bar{N}$. Acceptable BW correlation model fits should not only describe the correlation data but should maintain a small residual such that $\delta\bar{\rho}'(y_t) \ll \bar{\rho}_{\text{ch}}(y_t)$.

The complete two-particle distribution, whose marginal equals the measured single-particle charge distribution, must be adjusted from the original form in Eq. (30). The adjusted distribution is given by

$$
\begin{aligned}
\bar{\rho}_{\text{BW,se}}(y_{t1}, y_{t2}) &= \bar{\rho}'_{\text{BW,se}}(y_{t1}, y_{t2}) + \frac{\bar{N} - 1}{\bar{N}} \\
&\quad \times [\bar{\rho}_{\text{BW,marg}}(y_{t1})\delta\bar{\rho}'(y_{t2}) + \bar{\rho}_{\text{BW,marg}}(y_{t2}) \\
&\quad \times \delta\bar{\rho}'(y_{t1}) + \delta\bar{\rho}'(y_{t1})\delta\bar{\rho}'(y_{t2})],
\end{aligned} \tag{41}
$$

where the pair normalization factor $(\bar{N} - 1)/\bar{N}$ from Eq. (30) was applied to the last three terms. The uncorrelated reference pair distribution is defined as the product of marginals of

$\bar{\rho}_{\text{BW,se}}(y_{t1}, y_{t2})$ in Eq. (41), which is given by

$$\bar{\rho}_{\text{BW,ref}}(y_{t1}, y_{t2}) = \frac{\bar{N}-1}{\bar{N}}[\bar{\rho}_{\text{BW,marg}}(y_{t1})\bar{\rho}_{\text{BW,marg}}(y_{t2}) + \bar{\rho}_{\text{BW,marg}}(y_{t1})\delta\bar{\rho}'(y_{t2}) + \bar{\rho}_{\text{BW,marg}}(y_{t2})\delta\bar{\rho}'(y_{t1}) + \delta\bar{\rho}'(y_{t1})\delta\bar{\rho}'(y_{t2})]$$

$$= \frac{\bar{N}-1}{\bar{N}}\bar{\rho}_{\text{ch}}(y_{t1})\bar{\rho}_{\text{ch}}(y_{t2}), \tag{42}$$

where the pair normalization factor $(\bar{N}-1)/\bar{N}$ must also be applied to the reference as shown in Ref. [17]. The per-pair normalized correlation is finally given by

$$\frac{\Delta\bar{\rho}_{\text{BW}}}{\bar{\rho}_{\text{BW,ref}}}(y_{t1}, y_{t2}) \equiv \frac{\bar{\rho}_{\text{BW,se}}(y_{t1}, y_{t2}) - \bar{\rho}_{\text{BW,ref}}(y_{t1}, y_{t2})}{\bar{\rho}_{\text{BW,ref}}(y_{t1}, y_{t2})} = \frac{\bar{\rho}'_{\text{BW,se}}(y_{t1}, y_{t2}) - \frac{\bar{N}-1}{\bar{N}}\bar{\rho}_{\text{BW,marg}}(y_{t1})\bar{\rho}_{\text{BW,marg}}(y_{t2})}{\bar{\rho}_{\text{BW,ref}}(y_{t1}, y_{t2})}. \tag{43}$$

D. Correlation prefactor

The final BW correlation quantity to be compared with data includes a prefactor corresponding to that applied to the data [14]. In general, the purpose of a correlation prefactor is to replace the pair ratio in Eq. (43), which is required in data analysis to correct for efficiency and acceptance, with a quantity better suited to the study of specific scaling trends, e.g., binary scaling, per-trigger scaling, etc. A prefactor may also be required by the specific charge-pair combinations used, and the relative pseudorapidity and/or azimuthal angle selections.

In the present model, the specific purposes of the correlation prefactor are (1) to convert the number of correlated pairs per final-state *pair* quantity in Eq. (43) to a number of correlated pairs per final-state *particle* ratio as in Pearson's correlation coefficient [14,41]; (2) to scale this "pairs per singles" ratio to account for the fact that only one-half of the available charged-particle pairs are included when selecting only the away-side pairs whose relative azimuth angle $|\phi_1 - \phi_2|$ exceeds $\pi/2$ (away-side pairs were selected for the analytical model fitting in Ref. [13], and in the present analysis, in order to suppress contributions from HBT correlations [22]); and (3) to provide an overall normalization which facilitates tests of binary scaling in the correlation structures. The last requirement can be achieved by using the soft-QCD process particle yield, as estimated in the Kharzeev-Nardi [31] two-component model. In the KN model, soft-QCD yields are proportional to N_{part}, where N_{part} is the number of participant nucleons in the heavy-ion collision. If the number of correlated pairs in the numerator is proportional to the number of binary nucleon + nucleon $(N + N)$ interactions, N_{bin}, then the resulting correlation quantity will be proportional to $N_{\text{bin}}/N_{\text{part}}$. Ratio $N_{\text{bin}}/N_{\text{part}}$ is proportional to centrality measure $\nu \equiv N_{\text{bin}}/(N_{\text{part}}/2)$ [27]. Correlation structures which scale with N_{bin} will linearly increase with centrality measure ν and can therefore be readily identified.

For the present study, we use a charge-independent (CI, all charge-pair combinations), away-side azimuth (AS, $|\phi_1 - \phi_2| > \pi/2$), soft-process particle production prefactor, $\mathcal{P}_{\text{Fac,soft}}^{\text{AS-CI}}(y_{t1}, y_{t2})$. The final correlation quantity is given by

$$\frac{\Delta\bar{\rho}_{\text{BW}}}{\sqrt{\bar{\rho}_{\text{soft}}}}(y_{t1}, y_{t2}) \equiv \mathcal{P}_{\text{Fac,soft}}^{\text{AS-CI}}(y_{t1}, y_{t2})\frac{\Delta\bar{\rho}_{\text{BW}}}{\bar{\rho}_{\text{BW,ref}}}(y_{t1}, y_{t2}), \tag{44}$$

where the prefactor is defined and calculated in Appendix A and the last quantity is given in Eq. (43).

IV. TWO-COMPONENT FRAGMENTATION MODEL WITH FLUCTUATIONS

A. Single-particle distribution

The two-component fragmentation model presented here is based on the two-component multiplicity production model of Kharzeev and Nardi [31], discussed briefly in the preceding section. In this model, particle production is assumed to be dominated by two processes which scale with either N_{part} or N_{bin}. The relevance of this model in the description of the peaked correlation structures on (p_{t1}, p_{t2}) from $p + p$ collisions was discussed in Refs. [7,25]. In the KN model, the particle yield N within some (η, ϕ) acceptance is given by

$$N = n_{pp}(1 - x_{\text{KN}})N_{\text{part}}/2 + n_{pp}x_{\text{KN}}N_{\text{bin}}, \tag{45}$$

where $n_{pp} = 4.95$ is the charged-particle yield in $\sqrt{s} = 200$ GeV nonsingly diffractive, minimum-bias $p + p$ collisions at midrapidity within acceptance $\Delta\eta = 2$, full 2π azimuth, and $p_t > 0.15$ GeV/c [42]. Parameter x_{KN} is approximately 0.1 [42] for charged-particle production in $\sqrt{s_{NN}} = 200$ GeV minimum-bias Au+Au collisions within the preceding acceptance.

In the present application, we assume the N_{part}-scaling production derives from soft-QCD, longitudinal fragmentation of color-flux tubes [36]. Similarly, the N_{bin}-scaling production corresponds to semihard (few GeV) and hard (few tens of GeV) QCD, transversely fragmenting partons, or jets. For the present application, the N_{bin}-scaling production is dominated by the lower energy, semihard part of the spectrum [3]. Fluctuations are included in the following: (1) the p_t-distribution shape, e.g., overall slope parameter β_{cs}, for the charged-particle production from each longitudinally fragmenting color string [1,36]; (2) the energy of each semihard scattered parton and resulting jet; and (3) the relative number of "soft" and "semihard" produced particles per event.

For a collection of collision events within a centrality bin, the mean charged-particle yield in this model is given by

$$\bar{\rho}_{\text{ch}}(y_t) = \bar{\rho}_{\text{s}}(y_t) + \bar{\rho}_{\text{h}}(y_t) + \delta\bar{\rho}(y_t) \tag{46}$$

for "soft," "hard," and residual components, respectively. The soft-component production occurs via fragmentation of longitudinal color strings [1], which are assumed to produce

MB p_t distributions with fluctuating slope parameter β_{cs}. As in the BW model, we assume the probability distribution of parameter β_{cs} is given by a γ distribution, such that

$$\bar{\rho}_s(y_t) = \bar{N}_s \int d\beta_{cs} f_\gamma(\beta_{cs}, \bar{\beta}_{cs}, q_{\beta_{cs}}) \hat{\rho}_s(\beta_{cs}, y_t) \quad (47)$$

using the steps in Sec. II, where unit-normalized density $\hat{\rho}_s(\beta_{cs}, y_t) \propto \exp[-\beta_{cs}(m_t - m_0)]$. The resulting Levy distribution in Eq. (47) can be equated to the soft-production particle spectrum estimated in Appendix A, given by

$$\bar{\rho}_s(y_t) = \Delta\eta \frac{d^2 N_{\text{ch,soft}}}{dy_t d\eta}. \quad (48)$$

The mean multiplicity $\bar{N}_s$ in Eq. (47) is determined by the parameters in Table V in Appendix A.

The semihard component yield is produced by fragmenting partons (jets) whose total energy fluctuates from jet to jet. The jet energy is represented in terms of the maximum possible transverse rapidity, $y_{\max}$, of its final-state fragment particles. The probability distribution of $y_{\max}$ is given by QCD power-law distribution $\hat{g}(y_{\max})$, defined in Ref. [3] and given below. The fragment distribution on y_t for given jet parameter $y_{\max}$ is $\hat{\rho}_h(y_{\max}, y_t)$, which is also defined below. Using the steps in Sec. II, the event-average semihard single-particle yield distribution is given by

$$\bar{\rho}_h(y_t) = \bar{N}_h \int_0^\infty dy_{\max} \hat{g}(y_{\max}) \hat{\rho}_h(y_{\max}, y_t)$$
$$\equiv \bar{\rho}_{[g]}(y_t), \quad (49)$$

where in the last line we define the convolution integral with symbol $\bar{\rho}_{[g]}(y_t)$ for later use.

Quantity $\hat{g}(y_{\max})$ is the probability distribution for producing particles from a jet with maximum fragment rapidity $y_{\max}$ in a $N + N$ collision. In Ref. [3], this quantity is given by

a QCD power-law distribution with low momentum cutoff, multiplied by a quadratic yield increase factor $(y_{\max} - y_{\min})^2$ where $y_{\min}$ is an empirical fitting parameter given in Ref. [3]. The quadratically increasing yield results from the approximate shape-invariant evolution of the distribution of jet fragments observed at LEP in inclusive $e^+ + e^- \to \text{jet}(Q^2) + X$ production over a wide range of jet energies [3,43]. Probability distribution $\hat{g}(y_{\max})$ is therefore proportional to [3]

$$\hat{g}(y_{\max})$$
$$\propto \frac{1}{2}\sigma_{\text{dijet}}(n_{\text{QCD}} - 2)\left\{\tanh\left(\frac{y_{\max} - y_{\text{cut}}}{\xi_{\text{cut}}}\right) + 1\right\}$$
$$\times e^{-(n_{\text{QCD}} - 2)(y_{\max} - y_{\text{cut}})}(y_{\max} - y_{\min})^2, \quad (50)$$

where $\sigma_{\text{dijet}} = 2.5$ mb at $\sqrt{s} = 200$ GeV, and from Ref. [3] $n_{\text{QCD}} = 7.5$, $y_{\min} = 0.35$, and low-momentum cutoff parameters are $y_{\text{cut}} = 3.75$ and $\xi_{\text{cut}} = 0.1$.

Particle distribution $\hat{\rho}_h(y_{\max}, y_t)$ is proportional to the distribution deduced in Ref. [3] for $e^+ + e^- \to \text{jet} + X$ multiplied by a low-momentum jet-fragment suppression factor determined by analyzing the jet fragment distributions from $p + \bar{p} \to \text{jet} + X$ collisions [44]. Quantity $\hat{\rho}_h(y_{\max}, y_t)$ from Ref. [3] is proportional to

$$\hat{\rho}_h(y_{\max}, y_t) \propto \tanh\left(\frac{y_t - y_0}{\xi_y}\right)\frac{u^{\lambda-1}(1-u)^{\omega-1}}{B(\lambda, \omega)} \quad (51)$$

for $y_{\max} \geqslant y_t \geqslant y_0$, where the last factor is a normalized β distribution with

$$u \equiv \frac{y_t - y_{\min}}{y_{\max} - y_{\min}}, \ u \in [0, 1]. \quad (52)$$

Quantity $B(\lambda, \omega) = \Gamma(\lambda)\Gamma(\omega)/\Gamma(\lambda + \omega)$, where Γ is the Γ function.

Collecting terms, the above semihard process single-particle distribution becomes

$$\bar{\rho}_h(y_t) = \bar{N}_h \mathcal{N}_h \int_0^\infty dy_{\max} \frac{1}{2}\sigma_{\text{dijet}}(n_{\text{QCD}} - 2)\left\{\tanh\left(\frac{y_{\max} - y_{\text{cut}}}{\xi_{\text{cut}}}\right) + 1\right\}$$
$$\times e^{-(n_{\text{QCD}} - 2)(y_{\max} - y_{\text{cut}})}(y_{\max} - y_{\min})^2 \tanh\left(\frac{y_t - y_0}{\xi_y}\right)\Big|_{y_t \geqslant y_0} \frac{u^{\lambda-1}(1-u)^{\omega-1}}{B(\lambda, \omega)}\Big|_{y_{\min} \leqslant y_t \leqslant y_{\max}} \quad (53)$$

where $\mathcal{N}_h$ normalizes the integral of $\bar{\rho}_h(y_t)$ over all y_t bins to $\bar{N}_h$. Quantities in Eq. (53) are calculated at the midpoints of the y_t bins when comparing with data.

The two-component fragmentation model was applied to the charged-particle p_t spectrum data discussed in Sec. III. The semihard process particle production model in Eq. (53) was fitted to the difference distribution $\bar{\rho}_{\text{ch}}(y_t) - \bar{\rho}_s(y_t)$ in the y_t range from 1.34 to 4.36 as before by varying parameters n_{QCD}, the jet production cutoff y_{cut}, the soft-fragment cutoff $y_0 = \xi_y$, and fragment distribution parameters λ and ω in Eq. (51). Better fits were achieved by variation of the shape of the fragment distribution, via parameters λ and ω, than were obtained by varying the cutoff parameter y_0. The latter parameter was subsequently fixed to zero.

Best fits were attained via χ^2 minimization. Quantitative descriptions of the semihard component spectrum at the maximum peak and in the higher momentum tails were achieved for each centrality. Example fits to $\bar{\rho}_{\text{ch}}(y_t)$ are shown in Fig. 3 for the 60–80%, 20–30%, and 0–5% centralities. The TCF model parameters are listed for all centralities in Table II. Parameter n_{QCD} increases slightly and smoothly with centrality, increasing above the value (7.5) estimated in Ref. [3]. Jet production cutoff parameter y_{cut} is approximately constant and larger than the value (3.75) in Ref. [3]. The modifications of the fragment distribution [β distribution in Eq. (51)] relative to the nominal shape from Ref. [3] are also shown in the lower row of panels. The trends imply a softening of the fragment distribution (suppression at higher
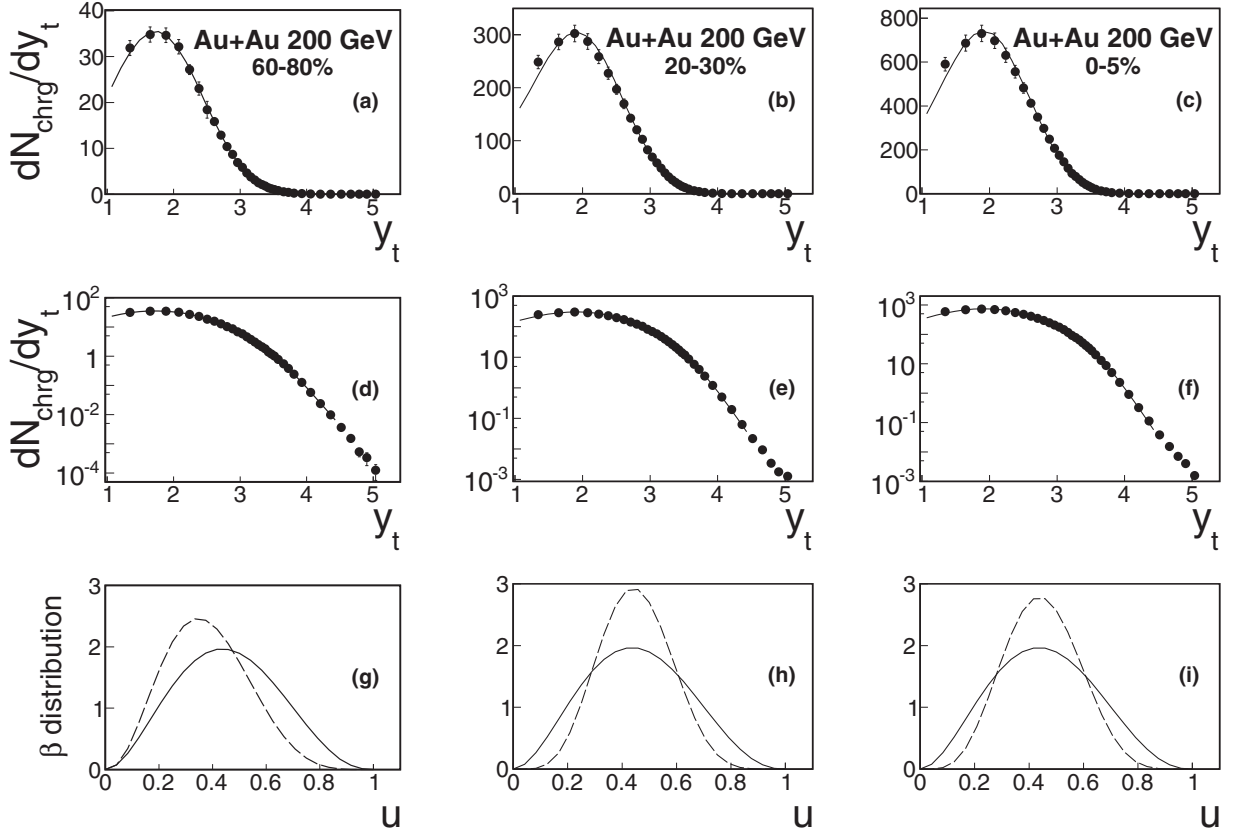
FIG. 3. Fluctuating TCF model fits to the 200-GeV Au+Au minimum-bias p_t spectrum data from STAR [40] (see text) showing only the 60–80%, 20–30%, and 0–5% centrality results. Combined soft plus semihard process yields are shown as quantity dN_{ch}/dy_t versus transverse rapidity y_t, assuming pseudorapidity acceptance $\Delta\eta = 2$. Linear (upper row) and semilog (middle row) plots are shown for the same data and model fits to allow visual access to the fit quality in both the lower and higher y_t ranges. Modifications to the fragment distribution for each centrality are shown in the lower row of panels where the nominal (solid lines) [3] and fitted (dashed lines) normalized β distributions are plotted vs transverse rapidity scaling variable u in Eq. (52).

p_t) coupled with a suppression at lower momentum relative to that observed in $e^+ + e^- \rightarrow$ jet $+ X$, which was discussed in Ref. [3] and which quickly develops with increasing collision centrality. The residuals vary from $\leqslant 2\%$ to $\leqslant 4\%$ of the charged-particle distribution from peripheral to most-central collisions, respectively, for $y_t < 3$. The residuals increase in

TABLE II. TCF model fit parameters for the 200-GeV Au+Au minimum-bias p_t spectra data from STAR [40] within $\Delta\eta = 2$ units acceptance. Data were fit in the y_t range from 1.34 to 4.36 using 30 data points at each centrality. Fit quality was insensitive to soft-fragment cutoff parameter y_0, which was subsequently set to zero.

Centrality(%)	$\bar{N}_s$	$\bar{N}_h$	n_{QCD}	y_{cut}	λ	ω	χ^2/DoF
0–5	649.2	479.5	9.1	4.3	5.6	6.9	1.632
5–10	555.1	354.9	9.0	4.3	5.9	7.0	1.823
10–20	433.1	256.7	8.55	4.35	5.95	7.3	1.042
20–30	308.4	160.0	8.35	4.4	6.2	7.6	0.957
30–40	215.2	98.8	8.1	4.45	6.25	7.85	1.266
40–60	110.8	53.4	7.6	4.3	4.7	6.4	0.665
60–80	36.1	16.6	7.15	4.25	3.5	5.7	0.410

relative magnitude at larger $y_t > 3$, varying from $\leqslant 3\%$ to $\leqslant 7\%$ of the charged-particle distribution from peripheral to most central collisions, respectively.

Conventional, theoretical applications of the TCF framework include eventwise fluctuations which cause the p_t spectra to vary event by event, resulting in nonzero correlations on transverse momentum. The Monte Carlo code HIJING [23], which combines the LUND model [1] and PYTHIA [2], includes fluctuating particle production from fragmenting color strings and minijets. AMPT [45] incorporates eventwise fluctuating initial conditions from HIJING and then includes stochastic parton propagation and interactions followed by hadronization.

B. Two-particle distribution

In the two-component fragmentation model, the two-particle distribution is generated by emissions from multiple color strings and from multiple jets in each heavy-ion collision. These processes are characterized by p_t slope parameters β_{cs_1} and β_{cs_2} and by jet parameters $y_{\max_1}$ and $y_{\max_2}$ for arbitrary particles 1 and 2, respectively. Correlations arise when the event-average probability distributions on $(\beta_{cs_1}, \beta_{cs_2})$ and

$(y_{\max_1}, y_{\max_2})$ are correlated. For example, a pair of particles emitted from the same color string, or from the same jet, are correlated in the sense that they share the same β_{cs} or $y_{\max}$, respectively. In the present application, correlated fluctuations between color string β_{cs} and jet $y_{\max}$ are not included as these are defined to be independent processes in this model. The two-particle same-event pair distribution in this model is given by

$$
\begin{aligned}
\bar{\rho}_{\mathrm{TCF,se}}&(y_{t1}, y_{t2}) \\
&= \frac{\bar{N}-1}{\bar{N}} \frac{1}{\epsilon} \sum_{j=1}^{\epsilon} [\rho_{s,j}(y_{t1}) + \rho_{h,j}(y_{t1}) + \delta\bar{\rho}(y_{t1})] \\
&\quad \times [\rho_{s,j}(y_{t2}) + \rho_{h,j}(y_{t2}) + \delta\bar{\rho}(y_{t2})] \qquad (54)
\end{aligned}
$$

$$
\begin{aligned}
&= \frac{\bar{N}-1}{\bar{N}} \frac{1}{\epsilon} \sum_{j=1}^{\epsilon} \{ \rho_{s,j}(y_{t1})\rho_{s,j}(y_{t2}) + \rho_{h,j}(y_{t1})\rho_{h,j}(y_{t2}) \\
&\quad + [\rho_{s,j}(y_{t1})\rho_{h,j}(y_{t2}) + \rho_{s,j}(y_{t2})\rho_{h,j}(y_{t1})] \\
&\quad + \delta\bar{\rho}(y_{t1})[\rho_{s,j}(y_{t2}) + \rho_{h,j}(y_{t2})] \\
&\quad + \delta\bar{\rho}(y_{t2})[\rho_{s,j}(y_{t1}) + \rho_{h,j}(y_{t1})] + \delta\bar{\rho}(y_{t1})\delta\bar{\rho}(y_{t2}) \} \\
&\equiv \bar{\rho}_{ss} + \bar{\rho}_{hh} + \bar{\rho}_{sh} + \bar{\rho}_{hs} + \bar{\rho}_{\delta}. \qquad (55)
\end{aligned}
$$

The color-string term, $\bar{\rho}_{ss}$, can be expanded as in Sec. II, where

$$
\begin{aligned}
\bar{\rho}_{ss}(y_{t1}, y_{t2}) &\equiv \frac{\bar{N}-1}{\bar{N}} \frac{N_{(2)s}}{\epsilon} \iint d\beta_{cs_1} d\beta_{cs_2} f(\beta_{cs_1}, \beta_{cs_2}) \\
&\quad \times \hat{\rho}_s(\beta_{cs_1}, y_{t1}) \hat{\rho}_s(\beta_{cs_2}, y_{t2}). \qquad (56)
\end{aligned}
$$

The average number of soft-particle pairs is

$$
\frac{N_{(2)s}}{\epsilon} = \bar{N}_s^2 + \sigma_s^2, \qquad (57)
$$

where σ_s^2 is the variance of the eventwise fluctuation in the number of particles emitted by color-string fragmentation. Correlated distribution $f(\beta_{cs_1}, \beta_{cs_2})$ is the same as in Eq. (34) and $\hat{\rho}_s(\beta_{cs}, y_t)$ is the unit-normalized MB distribution introduced in Eq. (47). The integral in Eq. (56) is given in Ref. [22] in terms of single-particle MB distributions on transverse mass m_t, where single-particle distributions on kinematic variables p_t, m_t, and y_t are related by

$$
\frac{d^2N}{dy_t d\eta} = 2\pi p_t \frac{dp_t}{dy_t} \frac{d^2N}{2\pi p_t dp_t d\eta} = 2\pi p_t m_t \frac{d^2N}{2\pi m_t dm_t d\eta}, \qquad (58)
$$

where $dp_t/dy_t \to m_t$ at midrapidity. The resulting two-particle distribution is given by

$$
\begin{aligned}
\bar{\rho}_{ss} &= \frac{\bar{N}-1}{\bar{N}} (\bar{N}_s^2 + \sigma_s^2) \mathcal{N}_{ss} \mathcal{J} \left(1 + \frac{\bar{\beta}_{cs} m_{t\Sigma}}{2q_{\beta_{cs\Sigma}}} \right)^{-2q_{\beta_{cs\Sigma}}} \\
&\quad \times \left[1 - \left(\frac{\bar{\beta}_{cs} m_{t\Delta}}{2q_{\beta_{cs\Delta}} + \bar{\beta}_{cs} m_{t\Sigma}} \right)^2 \right]^{-q_{\beta_{cs\Delta}}} \\
&\equiv \frac{\bar{N}-1}{\bar{N}} (\bar{N}_s^2 + \sigma_s^2) \hat{\rho}_{\mathrm{2D-Levy}}(y_{t1}, y_{t2}). \qquad (59)
\end{aligned}
$$

where $\mathcal{N}_{ss}$ is a normalization factor and $\mathcal{J} = 4\pi^2 p_{t1} m_{t1} p_{t2} m_{t2}$ is the Jacobian which transforms the

2D distribution on transverse mass to transverse rapidity. The unit-normalized 2D Levy distribution is defined in the last line of Eq. (59), which is calculated at the midpoints of the y_t bins when comparing to data. Also in the preceding equation kinematic variables $m_{t\Sigma} = m_{t1} + m_{t2} - 2m_0$ and $m_{t\Delta} = m_{t1} - m_{t2}$ were introduced. Relative variance difference quantities $\Delta(1/q)_{cs\Sigma,\Delta}$ and $\Delta(1/q)_{cs,\mathrm{Vol,cov}}$ are used in the fitting in analogy with similar quantities defined in Eqs. (35) and (36).

The hard-scattering term $\bar{\rho}_{hh}$ in Eq. (55) is similarly expanded as

$$
\begin{aligned}
\bar{\rho}_{hh}(y_{t1}, y_{t2}) &= \frac{\bar{N}-1}{\bar{N}} \frac{N_{(2)h}}{\epsilon} \iint dy_{\max_1} dy_{\max_2} \\
&\quad \times \hat{g}(y_{\max_1}, y_{\max_2}) \hat{\rho}_h(y_{\max_1}, y_{t1}) \hat{\rho}_h(y_{\max_2}, y_{t2}) \qquad (60)
\end{aligned}
$$

where the mean number of hard-scattering particle pairs is $\bar{N}_h^2 + \sigma_h^2$, where $\sigma_h^2 = \sigma_s^2$ when event multiplicities are constrained to fixed total $\bar{N}$. The unit-normalized, single-particle distribution $\hat{\rho}_h(y_{\max}, y_t)$ was defined in Eq. (51).

For the correlated distribution $\hat{g}(y_{\max_1}, y_{\max_2})$, a simplified functional form was assumed in order to reduce computational demands. The simplified function, $\hat{g}_2$ combines an uncorrelated (factorized) component and a fully correlated (diagonal) component defined by

$$
\begin{aligned}
\hat{g}_2(y_{\max_1}, y_{\max_2}) &= (1-\zeta) \hat{h}(y_{\max_1}) \hat{h}(y_{\max_2}) \\
&\quad + \zeta \hat{b}(y_{\max_1}) \delta(y_{\max_1} - y_{\max_2}), \qquad (61)
\end{aligned}
$$

where $0 \leqslant \zeta \leqslant 1$ is a fitting parameter, δ is the Dirac δ function,

$$
\hat{b}(y_{\max_1}) = \lim_{y_{\max_2} \to y_{\max_1}} \hat{g}'(y_{\max_1}) \hat{g}'(y_{\max_2}), \qquad (62)
$$

and $\hat{g}'(y_{\max})$ has the same form as $\hat{g}(y_{\max})$ in Eq. (50), but can have different parameter values. In taking the limit in the above equation, the product of the two hyperbolic tangent cutoff functions in both instances of $\hat{g}'$ is approximated by a single cutoff function with variable parameter $y_{\mathrm{cut}}^{\star}$. In addition, exponential argument $2(n_{\mathrm{QCD}} - 2)(y_{\max} - y_{\mathrm{cut}})$ is re-written as $(n_{\mathrm{QCD}}^{\star} - 2)(y_{\max} - y_{\mathrm{cut}}^{\star})$, where $n_{\mathrm{QCD}}^{\star}$ is freely varied in the fitting. The correlated portion of $\hat{g}_2(y_{\max_1}, y_{\max_2})$ becomes

$$
\begin{aligned}
\hat{b}(y_{\max_1}) &\delta(y_{\max_1} - y_{\max_2}) \\
&= \mathcal{N}_p \frac{1}{2} \left\{ \tanh\left(\frac{y_{\max_1} - y_{\mathrm{cut}}^{\star}}{\xi_{\mathrm{cut}}} \right) + 1 \right\} \\
&\quad \times e^{-(n_{\mathrm{QCD}}^{\star} - 2)(y_{\max_1} - y_{\mathrm{cut}}^{\star})} (y_{\max_1} - y_{\min})^4 \\
&\quad \times \delta(y_{\max_1} - y_{\max_2}) \qquad (63)
\end{aligned}
$$

with normalization constant $\mathcal{N}_p$. Correlations are generated in this model when $0 < \zeta \leqslant 1$ and may be modified by allowing $n_{\mathrm{QCD}}^{\star} \neq 2(n_{\mathrm{QCD}} - 1)$ and/or $y_{\mathrm{cut}}^{\star} \neq y_{\mathrm{cut}}$ where n_{QCD} and y_{cut} are determined by fitting the single-particle p_t spectra described in Sec. IV A.

It is essential that the single-particle projection (marginal) of $\bar{\rho}_{hh}$ equal the single-particle, semihard component $\bar{\rho}_h(y_t)$ [Eq. (49)] in order to maintain equality between the single-particle projection of the full, two-particle distribution in Eq. (55) and the measured charge distribution. This can be accomplished by requiring that

$$\int dy_{\max_2}\hat{g}_2\big(y_{\max_1}, y_{\max_2}\big) = \hat{g}\big(y_{\max_1}\big), \qquad (64)$$

which in turn requires that function $\hat{h}(y_{\max})$ in Eq. (61) be determined by

$$\hat{h}(y_{\max}) = [\hat{g}(y_{\max}) - \zeta\hat{b}(y_{\max})]/(1-\zeta), \zeta < 1 \quad (65)$$

as parameters $n^{\star}_{\text{QCD}}$ and $y^{\star}_{\text{cut}}$ in $\hat{b}(y_{\max})$ vary.

Substituting the above quantities into Eq. (60), where $\hat{g}(y_{\max_1}, y_{\max_2}) \longrightarrow \hat{g}_2(y_{\max_1}, y_{\max_2})$, results in the purely hard-scattering contribution to the same-event pair-distribution given by

$$\bar{\rho}_{hh}(y_{t1}, y_{t2}) = \frac{\bar{N}-1}{\bar{N}}\big(\bar{N}_h^2 + \sigma_s^2\big)\Bigg[(1-\zeta)\int dy_{\max_1}\hat{h}\big(y_{\max_1}\big)\hat{\rho}_h\big(y_{\max_1}, y_{t1}\big)\int dy_{\max_2}\hat{h}\big(y_{\max_2}\big)\hat{\rho}_h\big(y_{\max_2}, y_{t2}\big)$$

$$+ \zeta\int dy_{\max}\hat{b}(y_{\max})\hat{\rho}_h(y_{\max}, y_{t1})\hat{\rho}_h(y_{\max}, y_{t2})\Bigg]$$

$$\equiv \frac{\bar{N}-1}{\bar{N}}\big(\bar{N}_h^2 + \sigma_s^2\big)[(1-\zeta)\hat{\rho}_{[\text{h}]}(y_{t1})\hat{\rho}_{[\text{h}]}(y_{t2}) + \zeta\hat{\rho}_{\text{2D[b]}}(y_{t1}, y_{t2})], \qquad (66)$$

where $\hat{\rho}_{[\text{h}]}$ and $\hat{\rho}_{\text{2D[b]}}$ in the last line are defined by the integrals in the first two lines of the equation. As usual, the above quantities are calculated at the y_t bin midpoints.

The color-string, hard-scattering cross terms do not contribute to the correlations when β_{cs} and $y_{\max}$ fluctuations are independent. These terms are readily given by

$$\bar{\rho}_{sh} = \frac{\bar{N}-1}{\bar{N}}\big[1 - \sigma_s^2/(\bar{N}_s\bar{N}_h)\big]\bar{\rho}_s(y_{t1})\bar{\rho}_{[\text{g}]}(y_{t2}) \qquad (67)$$

using Eqs. (47) and (49) where the event-averaged number of "string-jet" pairs equals $(\bar{N}_s\bar{N}_h - \sigma_s^2)$ if the event multiplicity is fixed. Cross term $\bar{\rho}_{hs}$ is calculated by interchanging labels 1 and 2 in Eq. (67).

The remaining terms include products of the residual $\delta\bar{\rho}(y_t)$ with either $\bar{\rho}_s$, $\bar{\rho}_{[\text{g}]}$, or itself, and are collected into one term given by

$$\bar{\rho}_\delta \equiv \frac{\bar{N}-1}{\bar{N}}\{\delta\bar{\rho}(y_{t1})[\bar{\rho}_s(y_{t2}) + \bar{\rho}_{[\text{g}]}(y_{t2})]$$

$$+ \delta\bar{\rho}(y_{t2})[\bar{\rho}_s(y_{t1}) + \bar{\rho}_{[\text{g}]}(y_{t1})] + \delta\bar{\rho}(y_{t1})\delta\bar{\rho}(y_{t2})\}. \quad (68)$$

Combining terms $\bar{\rho}_{ss}$, $\bar{\rho}_{hh}$, $\bar{\rho}_{sh}$, $\bar{\rho}_{hs}$, and $\bar{\rho}_\delta$ gives $\bar{\rho}_{\text{TCF,se}}$ in Eq. (55).

C. Two-particle correlation and prefactor

The single-particle projection (marginal) of the two-particle distribution in Eq. (55) is given by

$$\bar{\rho}_{\text{TCF,marg}}(y_{t1})$$

$$= \frac{1}{\bar{N}-1}\int dy_{t2}\,\bar{\rho}_{\text{TCF,se}}(y_{t1}, y_{t2})$$

$$= \bar{N}_s\int dy_{t2}\,\hat{\rho}_{\text{2D-Levy}}(y_{t1}, y_{t2}) + \bar{\rho}_{[\text{g}]}(y_{t1}) + \delta\bar{\rho}(y_{t1}). \qquad (69)$$

If $|\Delta(1/q)_{cs,\text{Vol}}| \ll 1$, then the integral of $\hat{\rho}_{\text{2D-Levy}}$ over y_{t2} is accurately given by $\bar{\rho}_s(y_{t1})/\bar{N}_s$. The per-pair normalized correlation quantity is given by

$$\frac{\Delta\bar{\rho}_{\text{TCF}}}{\bar{\rho}_{\text{ref}}}(y_{t1}, y_{t2})$$

$$= \frac{\bar{\rho}_{\text{TCF,se}}(y_{t1}, y_{t2}) - \frac{\bar{N}-1}{\bar{N}}\bar{\rho}_{\text{TCF,marg}}(y_{t1})\bar{\rho}_{\text{TCF,marg}}(y_{t2})}{\bar{\rho}_{\text{ref}}(y_{t1}, y_{t2})}, \qquad (70)$$

analogous to Eq. (43) for the blast wave, where $\bar{\rho}_{\text{ref}}$ is defined as the product of marginals [see Eq. (42)]. It is given by

$$\bar{\rho}_{\text{ref}}(y_{t1}, y_{t2}) = \frac{\bar{N}-1}{\bar{N}}\bar{\rho}_{\text{TCF,marg}}(y_{t1})\bar{\rho}_{\text{TCF,marg}}(y_{t2}). \qquad (71)$$

Using the soft-process prefactor in Appendix A for the charge-independent, away-side azimuth pair correlations gives the final correlation for the two-component fragmentation model:

$$\frac{\Delta\bar{\rho}_{\text{TCF}}}{\sqrt{\bar{\rho}_{\text{soft}}}}(y_{t1}, y_{t2}) = \mathcal{P}^{\text{AS-CI}}_{\text{Fac,soft}}(y_{t1}, y_{t2})\frac{\Delta\bar{\rho}_{\text{TCF}}}{\bar{\rho}_{\text{ref}}}(y_{t1}, y_{t2}). \qquad (72)$$

Finally, it is instructive to expand $\Delta\bar{\rho}_{\text{TCF}}(y_{t1}, y_{t2})$ in terms of the separate sources of correlations built into the model. Inserting Eqs. (59) and (66)–(69) into $\Delta\bar{\rho}_{\text{TCF}}$ in Eq. (70) gives

$$\Delta\bar{\rho}_{\text{TCF}}(y_{t1}, y_{t2}) = \frac{\bar{N}-1}{\bar{N}}\Big\{\big(\bar{N}_s^2 + \sigma_s^2\big)\big[\hat{\rho}_{\text{2D-Levy}}(y_{t1}, y_{t2}) - \bar{\rho}_s(y_{t1})\bar{\rho}_s(y_{t2})/\bar{N}_s^2\big]$$

$$+ \big(\bar{N}_h^2 + \sigma_s^2\big)[(1-\zeta)\hat{\rho}_{[h]}(y_{t1})\hat{\rho}_{[h]}(y_{t2}) + \zeta\hat{\rho}_{\text{2D[b]}}(y_{t1}, y_{t2}) - \hat{\rho}_{[g]}(y_{t1})\hat{\rho}_{[g]}(y_{t2})]$$

$$+ \sigma_s^2[\bar{\rho}_s(y_{t1})/\bar{N}_s - \hat{\rho}_{[g]}(y_{t1})][\bar{\rho}_s(y_{t2})/\bar{N}_s - \hat{\rho}_{[g]}(y_{t2})]\Big\} \tag{73}$$

where $\hat{\rho}_{[g]} = \bar{\rho}_{[g]}/\bar{N}_h$. Soft string-fragmentation-induced correlations are represented in the first term and are controlled in the model via relative covariance parameter $\Delta(1/q)_{cs,\text{cov}} \equiv (1/2)[\Delta(1/q)_{cs\Sigma} - \Delta(1/q)_{cs\Delta}] = (1/q_{\beta_{cs\Sigma}} - 1/q_{\beta_{cs\Delta}})/2$, where the correlations scale with $(\bar{N}_s^2 + \sigma_s^2)$. The semihard scattering, correlated fragmentation contributions are represented in the second term, controlled by parameter $\zeta \in [0, 1]$, and modulated by the two-particle, correlated semihard scattering probability distribution parameters $y_{\text{cut}}^\star$ and $n_{\text{QCD}}^\star$ in function $\hat{b}(y_{\text{max}})$ [see Eq. (63)]. The semihard scattering correlations scale with $(\bar{N}_h^2 + \sigma_s^2)$. The semihard scattering versus soft string-fragmentation multiplicity fluctuation variance, σ_s^2, independently generates correlations when the soft and semihard particle distribution shapes differ as given by the third term in Eq. (73).

V. PHENOMENOLOGICAL MODEL CORRELATION RESULTS

The BW and TCF models were fitted to analytical representations of preliminary (y_{t1}, y_{t2}) charged-particle correlation data from STAR [13,14] described in Appendix B. We refer to these representations as "pseudodata." The fitting results are shown and discussed with respect to the efficacy of each model and the stability and systematic centrality dependencies of the model parameters. The centrality trends of the BW and TCF fitting parameters and some implications of those trends are discussed in the following subsections.

A. Blast-wave model description of correlations

The AS-CI correlation pseudodata were fitted with the fluctuating blast-wave model in Eq. (44) using fit parameters

$\Delta(1/q)_{\text{Vol}}$ and $\Delta(1/q)_{\text{cov}}$ in Eq. (36) plus the transverse flow correlation parameter Δ_{η_t} introduced just after Eq. (37). Other parameters of the model including $\bar{\beta} = 1/T$, q_β, a_0, n_{flow}, and σ_{η_t} were determined by fitting the single-particle p_t spectrum data (see Table I) and were kept fixed. Fit parameters and statistical fitting errors are listed in Table III. Pseudodata, BW model fits, and residuals (pseudodata − model) are shown for three example centrality bins (60–80%, 20–30%, and 0–5%) in Fig. 4. The results show smooth, monotonic centrality dependence from most peripheral to most central. The general features of the correlation structures, e.g., saddle-shape and peak near $(y_{t1}, y_{t2}) = (3, 3)$, are qualitatively reproduced by the model; however, the (3,3) peak amplitude is underestimated by about 20–30%. Residuals are somewhat smaller than the data overall, differing mainly at lower y_t and near the (3,3) peak.

The best determined fit parameter (smallest uncertainty) is the inverse temperature covariation $\Delta(1/q)_{\text{cov}}$ which is always positive, corresponding to positive correlations in the temperature fluctuations, and which displays a monotonic decrease with centrality. Of the three fit parameters, $\Delta(1/q)_{\text{cov}}$ has the smallest relative errors and displays the smoothest centrality trend. The overall (β_1, β_2) distribution expansion-contraction parameter $\Delta(1/q)_{\text{Vol}}$ tends to decrease (i.e., reduced fluctuations) with more central collisions. It has larger relative errors and greater variability than $\Delta(1/q)_{\text{cov}}$. The transverse flow rapidity correlation fit parameters $\Delta\eta_t$ are non-negative, indicating positive flow correlations, but have relatively large uncertainties and erratic centrality dependence, meaning that correlated transverse flow fluctuations are poorly determined with these fits.

An essential requirement of the BW correlation model is that the single-particle p_t distribution be preserved throughout the fitting process. In the BW model small, nonzero values

TABLE III. Blast-wave correlation model fit parameters to the 200-GeV Au+Au (y_{t1}, y_{t2}) AS-CI correlation pseudodata. Statistical fitting errors are listed in parentheses. Relative expansion or contraction and relative covariations in the thermal and transverse expansion parameters are also listed as explained in the text.

| Cent. (%)	$\Delta(1/q)_{\text{Vol}}$	$\Delta(1/q)_{\text{cov}}$	Δ_{η_t}	$\frac{\chi^2}{\text{DoF}}$	$\frac{\delta\sigma_\Sigma + \delta\sigma_\Delta}{2\bar{\beta}}$	$\frac{\delta\sigma_\Sigma - \delta\sigma_\Delta}{2\bar{\beta}}$	$\frac{\Delta_{\eta_t}}{2\sigma_{\eta_t}}$
0–5	−0.00162(38)	0.000500(4)	0.000400(135)	12.39	−0.00364	0.00112	0.0039
5–10	−0.00055(20)	0.000600(23)	0.0 ± 0.0009	14.46	−0.00122	0.00133	0
10–20	−0.00106(25)	0.000650(8)	0.00175(54)	26.64	−0.00229	0.00141	0.0265
20–30	−0.00160(43)	0.000850(21)	0.0 ± 0.0026	26.29	−0.00335	0.00178	0
30–40	−0.00100(39)	0.00110(4)	0.0 ± 0.0022	19.63	−0.00204	0.00225	0
40–60	+0.0020(6)	0.00140(5)	0.0 ± 0.0008	18.09	+0.00391	0.00274	0
60–80	+0.0100(4)	0.00210(5)	0.0030(61)	11.19	+0.018	0.00377	0.075
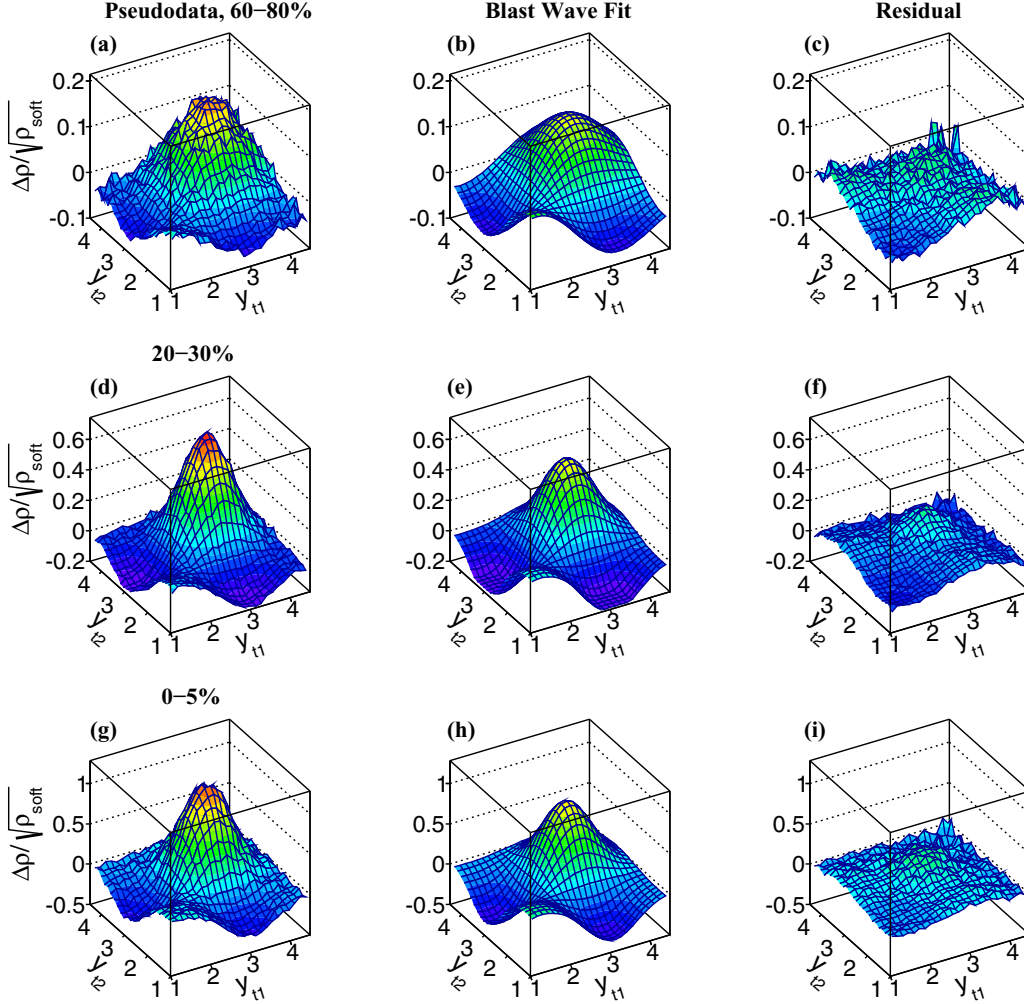
FIG. 4. Fluctuating blast-wave model fits to the 200-GeV Au+Au away-side, charge-independent two-particle correlation pseudodata described in Appendix B for selected centralities 60–80%, 20–30%, and 0–5% in rows of panels from upper to lower, respectively. The left-hand column shows the pseudodata, the fitted model results are shown in the middle column, and the residuals (pseudodata − model) are presented in the right-hand column.

of $\Delta(1/q)_{\mathrm{Vol}}$, which are beneficial in fitting the correlations, cause the marginal of the two-particle distribution [Eq. (39)] to differ from the single-particle BW model fit to the p_t spectrum data. For the present fits, however, the projections were consistent with the single-particle BW fits to within a few percent for all centralities except the most-peripheral 60–80% for $y_t \geqslant 3$.

It is interesting to examine the degree of correlation in the inverse temperature and transverse flow rapidity sampled by arbitrary pairs of particles. Ratio $\sigma_\beta^2 / \bar{\beta}^2$ is the relative variance of the inverse temperature distribution [Eq. (25)] for the single-particle distribution in Eq. (24). Defining $\delta\sigma_{\Sigma,\Delta}$ as the change in widths of the two-particle (β_1, β_2) distribution [see Fig. 2] along the $\beta_{\Sigma,\Delta} = \beta_1 \pm \beta_2$ directions, respectively, where $\delta\sigma_{\Sigma,\Delta} \equiv \sigma_{\beta_{\Sigma,\Delta}} - \sigma_\beta$, we estimate the average, relative expansion or contraction of the (β_1, β_2) distribution as

$$\frac{\delta\sigma_\Sigma + \delta\sigma_\Delta}{2\bar{\beta}} \approx (\sqrt{q_\beta}/2)\Delta(1/q)_{\mathrm{Vol}}, \qquad (74)$$

assuming $\delta\sigma_{\Sigma,\Delta}/\bar{\beta} \ll 1$. Similarly, the average, relative covariation in the (β_1, β_2) distribution is estimated by

$$\frac{\delta\sigma_\Sigma - \delta\sigma_\Delta}{2\bar{\beta}} \approx (\sqrt{q_\beta}/2)\Delta(1/q)_{\mathrm{cov}}. \qquad (75)$$

The average, relative covariation in the two-particle, transverse flow rapidity is equal to $\Delta_{\eta_t}/(2\sigma_{\eta_t})$. These three quantities are listed in Table III. The results show that, within this fluctuating BW model and for these AS-CI pseudodata, thermal fluctuation widths vary from about $+2\%$ increased overall fluctuation relative to that for single-particle production in peripheral collisions to about -0.4% (reduced fluctuations) in most-central collisions. The relative covariance decreases monotonically with centrality from about 0.4% to 0.1% from peripheral to most-central collisions. Transverse flow covariances are non-negative but display large variability with respect to collision centrality, showing no clear trend in these fitting results. These small, relative changes in widths of the inverse temperature and flow fluctuations imply that intraevent

β, η_{t0} fluctuation magnitudes exceed the mean differences in the interevent fluctuations as discussed in Ref. [22]. In other words, event-to-event fluctuations in the mean temperature and transverse flow are small relative to fluctuations within each collision system.

The BW model fits to the p_t spectrum data provide an estimate of the variance in the distribution of inverse p_t-slope parameters, e.g., temperature in the BW approach. It is informative to compare these empirical fluctuation magnitudes to that expected for fully equilibrated (uniform temperature), relativistic hadron-gas models at kinematic decoupling, or "freeze-out," when eventwise fluctuations in participant nucleon number alone are included. In relativistic hadron-gas models, the energy density ε is proportional to the freeze-out temperature to the fourth power [46], $\varepsilon \propto T^4$. In hydrodynamic models, the total energy available for hydrodynamic expansion among the interacting partons is proportional to the number of participant nucleons. At midrapidity, the energy density is therefore proportional to $N_{\text{part}}^{1/3}$ [33]. In hydrodynamic models, the energy density at freeze-out includes both thermal and collective modes, but it is still reasonable to assume that $T^4 \propto N_{\text{part}}^{1/3}$. Eventwise fluctuations in N_{part} among collisions having the same centrality, for example, as defined by the impact parameter or multiplicity, produce temperature fluctuations which, in turn, produce two-particle correlations on transverse momentum.

Numerical estimates can be carried out using the BW fit values for temperature from Table I and N_{part} from Table V. A proportionality constant, $\alpha = \partial T^4 / \partial N_{\text{part}}^{1/3} \approx 0.000015$ GeV^4, is estimated from the results if the most-peripheral bin is excluded. The resulting relation

$$\frac{\partial N_{\text{part}}}{\partial T} = 12 T^3 N_{\text{part}}^{2/3} / \alpha \approx \frac{\delta N_{\text{part}}}{\delta T}, \quad (76)$$

where δN_{part} and δT represent eventwise fluctuations, can be used to estimate the variance in the fluctuating global temperature at freeze-out caused by eventwise fluctuations in N_{part}. In terms of inverse temperature $\beta = 1/T$, the relative variance of fluctuations in β for a collection of similar events (e.g., same impact parameter) is given by

$$\langle (\delta \beta / \bar{\beta})^2 \rangle = \frac{\sigma_\beta^2}{\bar{\beta}^2} = \frac{1}{q_\beta} = \left[(12/\alpha)^2 T^8 N_{\text{part}}^{1/3} \right]^{-1}, \quad (77)$$

where brackets "$\langle \ \rangle$" denote an average over events, $\bar{\beta} = \langle \beta \rangle$, and the Poisson limit, $\langle (\delta N_{\text{part}})^2 \rangle = N_{\text{part}}$, was assumed.

Using the BW fitted temperatures in Eq. (77) and the above value of α, results in relative variances which are more than three orders of magnitude smaller than $1/q_\beta$ in Table I. The covariations in relative variance, $\Delta(1/q)_{\text{cov}}$ from the 2D BW model fits, are two orders of magnitude larger than the above limit in Eq. (77).

Both the β fluctuations required to describe the single-particle p_t distributions and the (β_1, β_2) covariances required to describe the correlations are much larger than what can be accounted for with statistical fluctuations in N_{part}. The present results imply that much stronger, dynamical fluctuations are required in hydrodynamic approaches and that β fluctuations within each collision event are much larger than eventwise fluctuations in mean β. Furthermore, the dynamical fluctuation effects must persist, to some extent, until kinetic freeze-out and cannot be completely dissipated, implying that final-state temperatures at kinetic freeze-out cannot be uniform. These results impose significant constraints on the initial state, on the effective partonic interactions in transport models, and on the parameters controlling hydrodynamic expansion.

B. Two-component fragmentation model description of correlations

The AS-CI correlation pseudodata were fit with the TCF model described in Sec. IV with parameters $\Delta(1/q)_{cs,\text{Vol,cov}} = (1/2)[\Delta(1/q)_{cs\Sigma} \pm \Delta(1/q)_{cs\Delta}]$ [see Eqs. (36) and (59)], semihard multiplicity fluctuation variance $\sigma_h^2 = \sigma_s^2$ in Eq. (57), semihard scattering correlation amplitude ζ in Eq. (61), and $\hat{b}(y_{\text{max}})$ probability distribution parameters $y_{\text{cut}}^\star$ and $n_{\text{QCD}}^\star$ in Eq. (63). Other parameters of the TCF model were determined by fitting the single, charged-particle p_t spectra data as discussed in Sec. IV, or were taken from Ref. [3].

Ambiguities occurred in the χ^2-minimization procedure in which discrete solutions were found for the color-string fragmentation parameter $\Delta(1/q)_{cs,\text{cov}}$ corresponding to a normal saddle-shape correlation (positive value) as in Ref. [22], or an inverted saddle-shape (negative value). An inherent assumption of the TCF model is that hadron fragments produced by the same color string will sample a p_t distribution with an overall slope (β_{cs}) whose value randomly fluctuates about a mean, resulting in a normal saddle-shape correlation with $\Delta(1/q)_{cs,\text{cov}} > 0$. Furthermore, it was found that acceptable descriptions of the correlations required relatively small absolute magnitudes for both $\Delta(1/q)_{cs,\text{Vol}}$ and

TABLE IV. Two-component fragmentation correlation model fit parameters to the 200-GeV Au+Au (y_{t1}, y_{t2}) AS-CI correlation pseudodata. Statistical fitting errors are in parentheses.

| Cent. (%)	$\Delta(1/q)_{cs,\text{Vol}}$	$\Delta(1/q)_{cs,\text{cov}}$	σ_s^2	ζ	$y_{\text{cut}}^\star$	$n_{\text{QCD}}^\star$	$\frac{\chi^2}{\text{DoF}}$
0–5	$-0.000285(47)$	$0.000415(60)$	620(87)	0.042(2)	4.06(4)	11.4(1.3)	11.3
5–10	$-0.000333(62)$	$0.000475(72)$	540(64)	0.051(3)	4.08(5)	11.8(1.8)	13.5
10–20	$-0.000382(62)$	$0.000535(70)$	310(39)	0.061(2)	4.12(4)	11.5(1.4)	22.7
20–30	$-0.000449(115)$	$0.000631(68)$	190(17)	0.072(3)	4.16(6)	11.6(2.2)	22.7
30–40	$-0.000635(144)$	$0.000876(92)$	115(11)	0.102(4)	4.22(9)	11.8(3.8)	17.0
40–60	$-0.001106(492)$	$0.001452(110)$	31(7)	0.158(6)	4.06(11)	11.6(4.8)	13.8
60–80	$-0.001964(1440)$	$0.002556(157)$	51(9)	0.44(3)	4.18(18)	11.6(7.4)	9.4
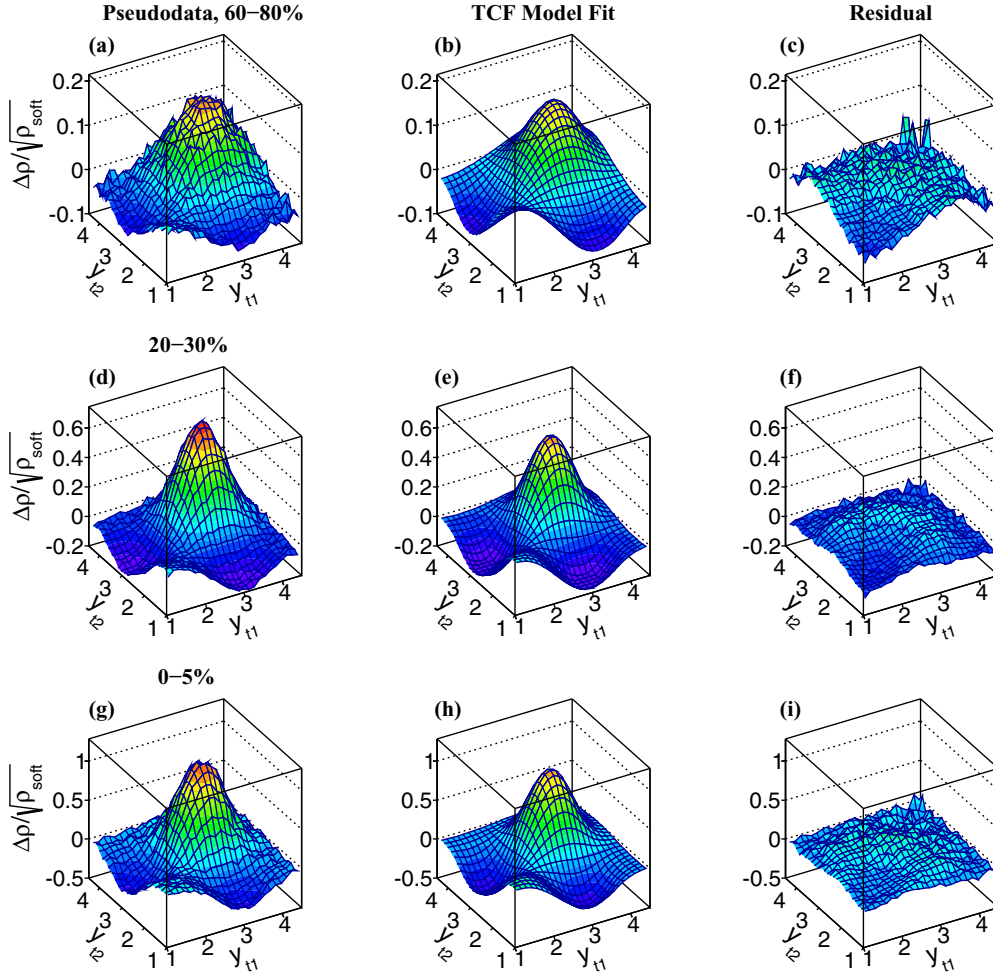
FIG. 5. Same as Fig. 4 except for the TCF model.

$\Delta(1/q)_{cs,\mathrm{cov}}$, similar to, or smaller than the corresponding 2D BW parameters in Table III. To adhere to these restrictions on $\Delta(1/q)_{cs,\mathrm{Vol,cov}}$ and stabilize the χ^2 minimization, we fixed the $\Delta(1/q)_{cs,\mathrm{Vol,cov}}$ parameters to the fitted values given in Ref. [14] (see Appendix B). With the soft-component thus constrained, the correlation pseudodata were readily described by varying the remaining semihard scattering parameters σ_s^2, ζ, $y_{\mathrm{cut}}^\star$, and $n_{\mathrm{QCD}}^\star$.

The model fits and residuals are compared with the correlation pseudodata in Fig. 5, and the fit parameters are listed in Table IV. Smooth, monotonic trends in the residuals and good, overall descriptions of the pseudodata were achieved. The fitted peak amplitudes at $(y_{t1}, y_{t2}) \approx (3, 3)$ are about 10% below the pseudodata. Color-string fragmentation parameters $\Delta(1/q)_{cs,\mathrm{Vol}}$ [14] are negative, indicating a slight, overall contraction in the widths of the distribution of p_t-slope parameter β_{cs}. This reduction is sufficiently small such that the marginals of the two-particle distributions remain within 1% of the charged-particle distributions over the full y_t range [1.0,4.5] for all centralities from 0 to 80%. Parameters $\Delta(1/q)_{cs,\mathrm{cov}}$ from Ref. [14] monotonically decrease from peripheral to most-central collisions, as was also found for the BW model fits (Table III), where similar numerical values were found.

Semihard scattering parameters σ_s^2 and ζ monotonically increase and decrease, respectively, from peripheral to most-central collisions, while parameters $y_{\mathrm{cut}}^\star$ and $n_{\mathrm{QCD}}^\star$ remain approximately constant with centrality. From the definition of the jet energy correlation function $\hat{b}(y_{\mathrm{max}})$ in Eq. (63), we expect $n_{\mathrm{QCD}}^\star \approx 2(n_{\mathrm{QCD}} - 1)$ in the weak correlation limit. The fitted values of $n_{\mathrm{QCD}}^\star$ vary from about 11 to 12, which are smaller than this estimated range that varies from 12 to 16 using the values for n_{QCD} in Table II. This indicates that the distributions of correlated, semihard scattering maximum fragment rapidities, represented by distribution $\hat{b}(y_{\mathrm{max}})$, are weighted toward larger y_{max} values (more energetic jets) than the corresponding single-particle distribution $\hat{g}(y_{\mathrm{max}})$. Or, in other words, positively correlated jet fragment pairs are more likely to be associated with higher energy jets, rather than lower. Overall, these results demonstrate that the TCF model is capable of providing qualitative descriptions of correlation data on transverse momentum resulting in smooth, monotonic centrality dependence in each of the fitting parameters.

In Eq. (73), contributions to the correlated pair distribution $\Delta\bar{\rho}_{\mathrm{TCF}}(y_{t1}, y_{t2})$ were separated into color-string fragmentation, semihard parton fragmentation, and semihard multiplicity fraction fluctuations. Neglecting the relatively small

centrality dependence in the shape of the single-particle distribution $\hat{\rho}_{[g]}(y_t)$, the centrality dependence of the last contribution in Eq. (73) is approximately proportional to hard-scattering multiplicity variance $\sigma_h^2 = \sigma_s^2$. The centrality dependence of σ_s^2 from Table IV is approximately described by a power law where

$$\sigma_s^2 \approx 0.17 N_{\text{bin}}^{1.19} \tag{78}$$

for the centrality range 0–60%. This distribution somewhat exceeds binary scaling. The second contribution in Eq. (73) can be expanded in powers of ζ, which to leading order is given by the combination of terms

$$\frac{\bar{N}-1}{\bar{N}}\big(\bar{N}_h^2 + \sigma_s^2\big)\zeta$$
$$\times\{[\hat{\rho}_{2D[b]}(y_{t1}, y_{t2}) - \hat{\rho}_{[b]}(y_{t1})\hat{\rho}_{[b]}(y_{t2})]$$
$$+ [\hat{\rho}_{[g]}(y_{t1}) - \hat{\rho}_{[b]}(y_{t1})][\hat{\rho}_{[g]}(y_{t2}) - \hat{\rho}_{[b]}(y_{t2})]\}, \tag{79}$$

where $\hat{\rho}_{[b]}$ is defined in analogy to Eq. (49) and using Eq. (65) is given by

$$\hat{\rho}_{[b]}(y_t) \equiv \int_0^\infty dy_{\max}\, \hat{b}(y_{\max})\hat{\rho}_h(y_{\max}, y_t)$$
$$= \frac{1}{\zeta}[\hat{\rho}_{[g]}(y_t) - (1 - \zeta)\hat{\rho}_{[h]}(y_t)]. \tag{80}$$

If the small centrality dependences of $\hat{\rho}_{[g]}(y_t)$ and $\hat{\rho}_{[b]}(y_t)$ are neglected, the number of correlated pairs in this contribution is approximately proportional to $(\bar{N}_h^2 + \sigma_s^2)\zeta \approx \bar{N}_h^2\zeta$. From Table IV, we find that for the 0–40% more central collisions, where ζ becomes smaller, the dependence of $(\bar{N}_h^2 + \sigma_s^2)\zeta$ can be approximated by

$$\big(\bar{N}_h^2 + \sigma_s^2\big)\zeta \approx 0.43 N_{\text{bin}}^{1.44}. \tag{81}$$

Thus, we find that empirical descriptions of the AS-CI correlation pseudodata, in terms of the TCF model, are consistent with a scenario in which the number of correlated particle pairs from semihard scattering and fragmentation processes increases smoothly with centrality and at a rate somewhat in excess of $N + N$ binary scaling.

The contributions of the three terms in Eq. (73) for the 60–80%, 20–30%, and 0–5% centrality bins are shown in Fig. 6 in comparison with the correlation pseudodata. For the pure color-string fragmentation contribution, parameters σ_s^2 and ζ were set to zero. For the pure semihard multiplicity fluctuation result, parameters $\Delta(1/q)_{cs,\text{Vol}}$, $\Delta(1/q)_{cs,\text{cov}}$, and ζ were set to zero. For the pure semihard fragmentation result, $\Delta(1/q)_{cs,\text{Vol}}$, $\Delta(1/q)_{cs,\text{cov}}$, and σ_s^2 were set to zero. The results accurately represent the contributions of the first two terms in Eq. (73) to the extent that $\sigma_s^2 \ll \bar{N}_s^2$ and $\sigma_s^2 \ll \bar{N}_h^2$, which are true at the 1% amount or better (see Tables II and IV), except for the 60–80% results. The color-string fragmentation contributes from about 20% of the predicted correlation peak amplitude at $(y_{t1}, y_{t2}) \approx (3, 3)$ in most-peripheral collisions to about 9% in most-central collisions. The semihard scattering contributions [last two terms in Eq. (73)] together account for the remaining 80% to 91% of the predicted correlation peak in 60–80% and 0–5% centrality bins, respectively. The semihard parton

fragmentation contribution ($\zeta > 0$) dominates the correlation peak at (3,3) in more central collisions.

VI. SUMMARY AND CONCLUSIONS

The study of relativistic heavy-ion collisions has greatly benefited from the plethora of two-particle correlation measurements and analysis over many years [6]. The vast majority of these correlation studies has focused on angular correlations. On the other hand, complementary correlation measurements on 2D transverse momentum are relatively scarce in the literature. In our opinion, the scientific impact of the correlations on transverse momentum which do exist has been diminished by the lack of available theoretical predictions and the absence of phenomenologically based interpretations.

To address this deficiency, we developed two phenomenological models based on fundamentally different frameworks for describing the dynamical evolution of the heavy-ion collision system. The first is based on hydrodynamic expansion as parametrized in the blast-wave model in which pairwise correlated fluctuations in the temperature and transverse flow at kinematic freeze-out are included in order to generate two-particle correlations in the final state. The second model is based on soft-QCD, longitudinal color-string fragmentation and semihard QCD, transverse scattering, and fragmentation in which fluctuations occur in the energies of the color strings and in the four-momentum transfer in the QCD scatterings, as well as in the relative numbers of particles produced via soft and semihard processes.

We demonstrated that both models are capable of quantitatively describing the measured charged-particle p_t spectra produced in $\sqrt{s_{\text{NN}}} = 200$ GeV Au+Au minimum-bias collisions. Using analytic representations of preliminary two-particle correlations on 2D transverse rapidity from the STAR Collaboration [13,14], we further demonstrated that both models are capable of qualitatively describing the correlations, resulting in smooth, monotonic centrality-dependent trends in most of the model parameters. The phenomenological model parameters and their resulting centrality trends can be interpreted in terms of the dynamical processes inherent in each model.

The results of this "proof of principle" study already provide some physical insight and impose constraints on the two dynamical frameworks considered here. In the hydrodynamic, BW approach, we found that statistical fluctuations in the number of participant nucleons from event to event, as the sole source of final-state fluctuations in the p_t distribution, are much too small to account for the observed correlation structures. Much larger, dynamical fluctuations are required whose effects must persist until kinetic freeze-out, thus restricting the degree of dissipation in the collision medium. The BW results also imply that the magnitudes of intraevent temperature fluctuations far exceed the interevent fluctuations in the mean temperature. This result may, for example, limit the allowed spatial scale for local, thermodynamic equilibrium in such models.

In the two-component fragmentation approach, we found that the semihard scattering and fragmentation-induced correlations required to describe the data appear to exceed binary
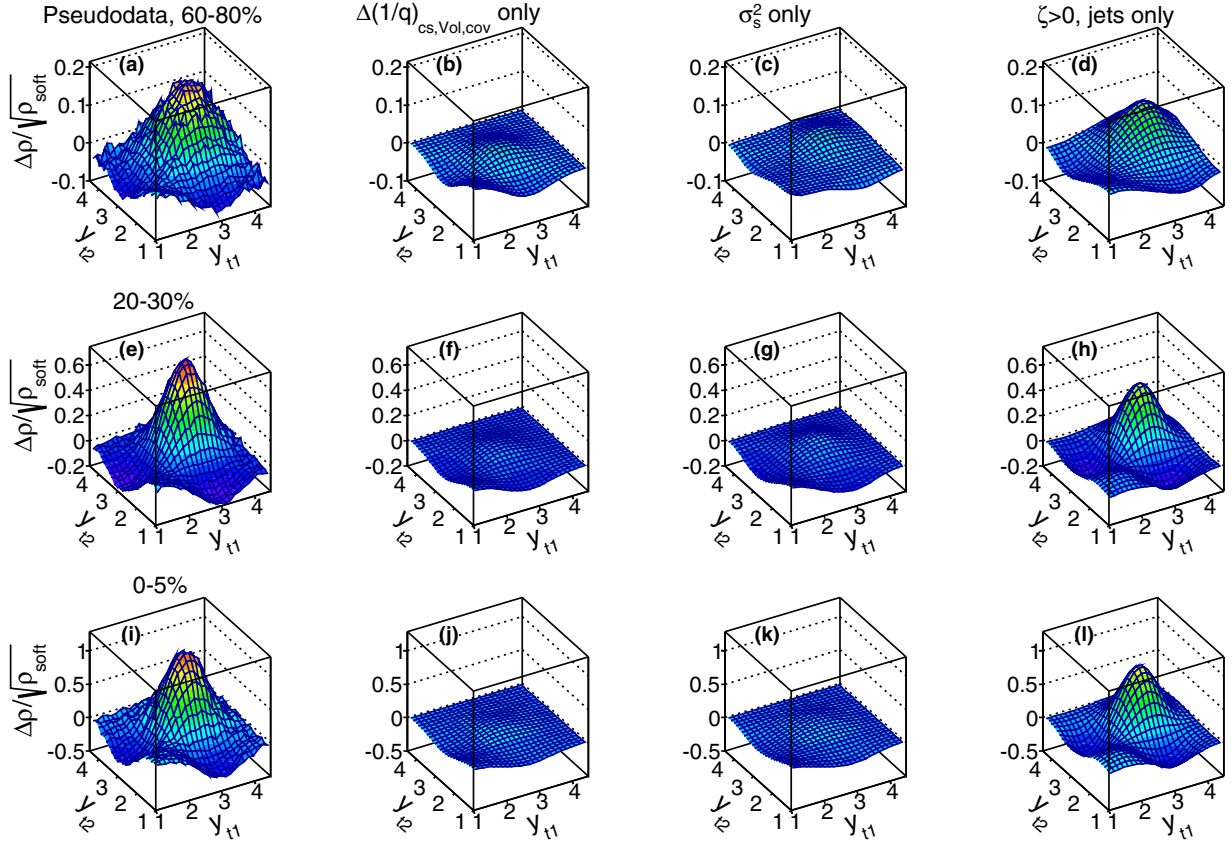
FIG. 6. Separate contributions to the fluctuating TCF model fits to the 200-GeV Au+Au away-side, charge-independent two-particle correlation pseudodata for selected centralities 60–80%, 20–30%, and 0–5% in rows of panels from upper to lower, respectively. The left-hand column of panels shows the pseudodata. Fluctuation contributions from color strings, semihard multiplicity production, and semihard fragmentation are shown in the second, third, and fourth columns of panels, respectively, as explained in the text.

scaling, which suggests additional, multiparton dynamics are required in the initial state or during fragmentation within the dense medium. We also found that in more central collisions the peak correlation structure at $(y_{t1}, y_{t2}) \approx (3, 3)$ is dominated by semihard parton fragmentation (minijets).

The connection between physical properties of the heavy-ion collision medium, e.g., temperature and flow velocity, inferred from analysis of single-particle p_t spectrum data, and eventwise fluctuations was emphasized. Using the BW model, we showed that fluctuations in the temperature and transverse flow affect the inferred, mean temperature and flow velocity by as much as a factor of two. Physical parameters inferred from fits to spectrum data using models without fluctuations are questionable.

The BW and TCF phenomenological models developed here can be used in future analyses of two-particle correlation measurements on transverse momentum or transverse rapidity to facilitate physical interpretation of the correlation structures and to better constrain theoretical models. Both phenomenologies can be used to estimate the magnitude and type of fluctuations required, within their respective frameworks, to describe correlation data. The magnitudes and centrality trends of those required fluctuations can be compared to the capabilities of theoretical models for producing such fluctuations. In this way, phenomenological analysis of two-particle correlations

on transverse momentum may enable more informed estimates of the validity of different theoretical approaches for understanding relativistic heavy-ion collisions.

APPENDIX A

The soft-reference prefactor for away-side pairs and all charged particles is given by

$$\mathcal{P}_{\text{Fac,soft}}^{\text{AS}-\text{CI}} \equiv \frac{1}{\sqrt{2}} \frac{\frac{d^2N_{\text{ch}}}{dy_{t1}d\eta_1}\frac{d^2N_{\text{ch}}}{dy_{t2}d\eta_2}}{\left[\frac{d^2N_{\text{ch,soft}}}{dy_{t1}d\eta_1}\frac{d^2N_{\text{ch,soft}}}{dy_{t2}d\eta_2}\right]^{1/2}}, \tag{A1}$$

where the distributions are calculated at the midpoints of each y_t bin and factor $1/\sqrt{2}$ accounts for using only away-side pairs. In this equation, the charged particle distribution was

TABLE V. Levy model fit parameters to the STAR Collaboration 200-GeV Au+Au minimum-bias charged-particle p_t spectra data in Ref. [40] in the range $y_t \in [1.34, 4.36]$. Also listed are the number of participant nucleons, number of binary $N + N$ collisions, and centrality measure ν [27]. The estimated soft-process p_t spectrum Levy model parameters in Eq. (A3) are $A_{\text{soft}} = 5.81 \ (c/\text{GeV}^2)$, $T_{\text{soft}} = 0.169 \, \text{GeV}$, and $q_{\text{soft}} = 13.8$.

Centrality (%)	ν	N_{part}	N_{bin}	A_{ch} (c/GeV^2)	T_{ch} (GeV)	q_{ch}
0–5	5.95	350.3	1042	1154.8	0.2176	17.41
5–10	5.50	299.5	824	935.8	0.2167	17.15
10–20	4.98	233.7	582	724.2	0.2129	16.00
20–30	4.34	166.4	361	503.4	0.2090	15.09
30–40	3.75	116.1	218	350.3	0.2036	14.28
40–60	2.87	59.8	85.7	205.76	0.1882	12.49
60–80	1.97	19.5	19.2	77.96	0.1695	11.06

parametrized with a Levy distribution where

$$\frac{d^2 N_{\text{ch}}}{dy_t d\eta} = 2\pi p_t \frac{dp_t}{dy_t} \left[\frac{d^2 N_{\text{ch}}}{2\pi p_t dp_t d\eta} \right]$$
$$= \frac{2\pi p_t m_t A_{\text{ch}}}{[1 + (m_t - m_0)/(T_{\text{ch}} q_{\text{ch}})]^{q_{\text{ch}}}}. \quad \text{(A2)}$$

Fit parameters A_{ch}, T_{ch}, and q_{ch} for the 200-GeV Au+Au spectra data reported by the STAR Collaboration [40] were determined in the y_t range from 1.34 to 4.36, corresponding to $p_t \in [0.25, 5.5] \, \text{GeV}/c$, and are listed in Table V. The N_{part} scaling, Kharzeev and Nardi soft-QCD process spectrum was also parametrized with the Levy distribution and is given by

$$\frac{d^2 N_{\text{ch,soft}}}{dy_t d\eta} = \frac{2\pi p_t m_t A_{\text{soft}} (N_{\text{part}}/2)}{[1 + (m_t - m_0)/(T_{\text{soft}} q_{\text{soft}})]^{q_{\text{soft}}}}. \quad \text{(A3)}$$

The number of participants for 200-GeV Au+Au minimum-bias collisions was estimated in Ref. [27] and interpolated to the present centrality bins (see Table V). A method for estimating the N_{part} scaling, soft-QCD process spectrum was presented in Ref. [42]. In the present analysis, the soft-QCD distribution was estimated by extrapolating the STAR [40] and PHENIX [47] Collaborations' p_t spectra data in each p_t bin to the $\nu \to 1$, $N + N$ collision limit and fitting the resulting distribution with the Levy model in Eq. (A3). The resulting fits gave $A_{\text{soft}} = 5.81 \ (c/\text{GeV}^2)$, $T_{\text{soft}} = 0.169 \, \text{GeV}$, and $q_{\text{soft}} = 13.8$.

APPENDIX B

Analytic representations of preliminary charged-particle correlations on (y_{t1}, y_{t2}) are described here and in Refs. [13,14]. Preliminary, charged-particle correlations on (y_{t1}, y_{t2}) in the range $y_t \in [1.0, 4.5]$ for minimum-bias Au+Au collisions at $\sqrt{s_{NN}} = 200 \, \text{GeV}$ from the STAR Collaboration were reported by Oldag [13,14]. The same-event and mixed-event pair densities were both normalized to the total number of pairs, as this analysis predates the methods developed in Ref. [17]. The data were fitted with a 2D-Levy distribution [Eq. (59)] plus a constant

offset and a 2D Gaussian. The correlations described with this model include all away-side, charged-pair combinations. The AS angular selection eliminates the enhanced correlation structure along the $y_{t1} = y_{t2}$ main-diagonal caused by quantum correlations between identical bosons [5] as discussed in Ref. [22]. The analytical fitting function is given by

$$\frac{\Delta\rho}{\sqrt{\rho_{\text{soft}}}}\bigg|_{\text{AS-CI}} = \mathcal{P}_{\text{Fac,soft}}^{\text{AS-CI}} \left(\frac{\hat{\rho}_{\text{2D-Levy}}^{\text{data}} - \hat{\rho}_{\text{2D-mix}}}{\hat{\rho}_{\text{2D-mix}}} \right)$$
$$+ A_0 + A_1 e^{-y_{t\Delta}^2/2\sigma_\Delta^2} e^{-(y_{t\Sigma} - 2y_{t0})^2/2\sigma_\Sigma^2}, \quad \text{(B1)}$$

where the 2D-Levy distribution is the same as in Eq. (59) with parameters β_0, q_Σ, and q_Δ in Ref. [14] replacing parameters $\bar{\beta}_{cs}$, $q_{\beta_{cs}\Sigma}$, and $q_{\beta_{cs}\Delta}$ in Eq. (59). The corresponding variance difference quantities are given by $\Delta(1/q)_{\Sigma,\Delta} = 1/q_{\Sigma,\Delta} - 1/q_{\text{fluct}}$. Also in Eq. (B1) we introduced sum and difference variables $y_{t\Sigma,\Delta} = y_{t1} \pm y_{t2}$. The marginal of $\hat{\rho}_{\text{2D-Levy}}^{\text{data}}$ is given by

$$\hat{\rho}_{\text{marg}}(y_{t1}) = \int dy_{t2} \, \hat{\rho}_{\text{2D-Levy}}^{\text{data}}(y_{t1}, y_{t2}) \quad \text{(B2)}$$

and the mixed-event reference $\hat{\rho}_{\text{2D-mix}}(y_{t1}, y_{t2})$ is the product of marginals for particles 1 and 2.

The 2D-Levy distribution alone did not produce satisfactory descriptions of the data and was supplemented with a constant offset (A_0) plus a 2D Gaussian. Fit parameters $\Delta(1/q)_{\Sigma,\Delta}$, q_{fluct}, A_0, A_1, y_{t0}, σ_Δ, and σ_Σ were interpolated from the trends plotted in Fig. 5.14 of Ref. [14], at the midpoints of the centrality bins studied here. The 2D Gaussian widths along the difference direction $y_{t\Delta}$ exceeded the corresponding widths along $y_{t\Sigma}$. Physically, for the AS correlations, this could be caused by initial-state transverse momentum, K_T, in the parton-parton collision frame which would impart more p_t to the fragments of one jet than the other, resulting in a broadening along $y_{t\Delta}$ when averaged over many dijets. Such additional, initial-state dynamics could be included in both the BW and TCF models but, for simplicity, was not accounted for in this initial "proof-of-principle" model study. The width σ_Δ in the pseudodata was therefore set equal to σ_Σ.

The correlation pseudodata were assigned statistical errors corresponding to the number of pairs per bin expected for the 9.5 million, 200-GeV minimum-bias Au+Au collisions in the data volume reported in Ref. [14] for the observed charged-particle p_t, η distributions in centrality bins 0–5%, 5–10%, 10–20%, 20–30%, 30–40%, 40–60%, and 60–80% and for single-particle acceptance $|\eta| \leqslant 1$, $p_t \geqslant 0.15 \, \text{GeV}/c$, full 2π azimuth, and assuming symmetric correlations with respect to $\pm|y_{t1} - y_{t2}|$. The latter symmetrization is valid when particles 1 and 2 are taken from the same collection of particles, for example, all charged particles. This step was implemented by counting each unique particle pair in both bins with coordinates (y_{t1}, y_{t2}) and (y_{t2}, y_{t1}). For diagonal bins (y_t, y_t), only the $y_{t1} \geqslant y_{t2}$ half was used for calculating the statistical errors. Typical statistical errors (for $y_t \leqslant 3$) in more central collisions vary from approximately 1% to 3% relative to the correlation amplitude at the peak near

$(y_{t1}, y_{t2}) = (3, 3)$. The errors increase to the range 3% to 5% in more peripheral collisions. The pseudodata were generated in each (y_{t1}, y_{t2}) bin by sampling a Gaussian distribution whose mean equals the calculated value in Eq. (B1) and whose width parameter (σ) was equal to the estimated

statistical error. The correlation pseudodata were binned on a uniform 25×25 2D grid for $y_t \in [1.0, 4.5]$ corresponding to $p_t \in [0.16, 6.3]\,\text{GeV}/c$. Pseudodata were generated for (y_{t1}, y_{t2}) bins with $y_{t1} \geqslant y_{t2}$, and then copied to the (y_{t2}, y_{t1}) bin.

[1] B. Andersson, G. Gustafson, G. Ingelman, and T. Sjöstrand, Phys. Rep. **97**, 31 (1983).

[2] T. Sjöstrand and M. van Zijl, Phys. Rev. D **36**, 2019 (1987).

[3] T. A. Trainor, Phys. Rev. C **80**, 044901 (2009); T. A. Trainor and D. T. Kettler, Phys. Rev. D **74**, 034012 (2006).

[4] D. Teaney, J. Lauret, and E. V. Shuryak, Phys. Rev. Lett. **86**, 4783 (2001); P. F. Kolb, U. Heinz, P. Huovinen, K. J. Eskola, and K. Tuominen, Nucl. Phys. A **696**, 197 (2001); U. Heinz, J. Phys. G: Nucl. Part. Phys. **31**, S717 (2005); P. Huovinen and P. V. Ruuskanen, Annu. Rev. Nucl. Part. Sci. **56**, 163 (2006).

[5] U. A. Wiedemann and U. Heinz, Phys. Rep. **319**, 145 (1999).

[6] T. A. Trainor, Int. J. Mod. Phys. E **23**, 1430011 (2014).

[7] T. A. Trainor and D. J. Prindle, Phys. Rev. D **93**, 014031 (2016).

[8] STAR Collaboration; J. Adams et al., Phys. Lett. B **634**, 347 (2006).

[9] ATLAS Collaboration; M. Aaboud et al., Phys. Rev. C **95**, 064914 (2017).

[10] STAR Collaboration, J. Adams et al., Phys. Rev. Lett. **95**, 152301 (2005).

[11] STAR Collaboration, J. Adams et al., J. Phys. G: Nucl. Part. Phys. **32**, L37 (2006).

[12] STAR Collaboration, J. Adams et al., J. Phys. G: Nucl. Part. Phys. **34**, 451 (2007).

[13] STAR Collaboration, E. W. Oldag, J. Phys.: Conf. Ser. **446**, 012023 (2013).

[14] E. W. Oldag, Ph.D. thesis, The University of Texas at Austin, Austin, TX, 2013 (unpublished), https://drupal.star.bnl.gov/STAR/files/oldag_dissertation_20132.pdf.

[15] P. Bhattarai, Ph.D. thesis, The University of Texas at Austin, Austin, TX, 2016 (unpublished), https://drupal.star.bnl.gov/STAR/files/PhDThesisPrabhat-3.pdf.

[16] D. T. Kettler, D. J. Prindle, and T. A. Trainor, Phys. Rev. C **91**, 064910 (2015).

[17] R. L. Ray and P. Bhattarai, Phys. Rev. C **94**, 064902 (2016).

[18] J. G. Reid, Nucl. Phys. A **698**, 611 (2002).

[19] NA49 Collaboration, S. V. Afanasiev et al., Nucl. Phys. A **715**, 55 (2003); NA49 Collaboration, T. Anticic et al., Phys. Rev. C **70**, 034902 (2004).

[20] CERES Collaboration, D. Adamová et al., Nucl. Phys. A **811**, 179 (2008).

[21] J. G. Reid, Ph.D. thesis, University of Washington, Seattle, WA, 2002 (unpublished), arXiv:nucl-ex/0302001.

[22] STAR Collaboration, J. Adams et al., J. Phys. G: Nucl. Part. Phys. **34**, 799 (2007).

[23] X.-N. Wang and M. Gyulassy, Phys. Rev. D **44**, 3501 (1991).

[24] STAR Collaboration, B. I. Abelev et al., Phys. Rev. C **79**, 034909 (2009).

[25] R. J. Porter and T. A. Trainor, J. Phys.: Conf. Ser. **27**, 98 (2005).

[26] L. Foà, Phys. Rep. C **22**, 1 (1975); J. Whitmore, ibid. **27**, 187 (1976).

[27] STAR Collaboration, G. Agakishiev et al., Phys. Rev. C **86**, 064902 (2012).

[28] STAR Collaboration, L. Adamczyk et al., Phys. Lett. B **751**, 233 (2015).

[29] E. Schnedermann, J. Sollfrank, and U. Heinz, Phys. Rev. C **48**, 2462 (1993).

[30] B. Tomášik, U. A. Wiedemann, and U. W. Heinz, Acta Phys. Hung. A **17**, 105 (2003).

[31] D. Kharzeev and M. Nardi, Phys. Lett. B **507**, 121 (2001); D. Kharzeev, E. Levin, and M. Nardi, Nucl. Phys. A **730**, 448 (2004).

[32] Z. Yang and R. J. Fries, J. Phys. Conf. Ser. **832**, 012056 (2017).

[33] J. D. Bjorken, Phys. Rev. D **27**, 140 (1983).

[34] PHOBOS Collaboration, B. B. Back et al., Phys. Rev. Lett. **91**, 052303 (2003).

[35] K. Werner, Nucl. Phys. B (Proc. Suppl.) **175–176**, 81 (2008).

[36] T. Lappi and L. McLerran, Nucl. Phys. A **772**, 200 (2006); F. Gelis and R. Venugopalan, Acta Phys. Polon. B **37**, 3253 (2006).

[37] M. Anderson et al., Nucl. Istrum. Meth. Phys. Res. A **499**, 659 (2003).

[38] Y. Hama, T. Kodama, and O. Socolowski Jr., Braz. J. Phys. **35**, 24 (2005); W.-L. Qian, R. Andrade, O. Socolowski Jr., F. Grassi, T. Kodama, and Y. Hama, ibid. **37**, 767 (2007).

[39] G. Wilk and Z. Włodarczyk, Phys. Rev. Lett. **84**, 2770 (2000).

[40] STAR Collaboration, J. Adams et al., Phys. Rev. Lett. **91**, 172302 (2003).

[41] J. L. Rodgers and W. A. Nicewander, Am. Stat. **42**, 59 (1988); B. S. Everitt and A. Skrondal, The Cambridge Dictionary of Statistics, 4th ed. (Cambridge University Press, Cambridge, UK, 2010), p. 107.

[42] T. A. Trainor, Int. J. Mod. Phys. E **17**, 1499 (2008).

[43] TASSO Collaboration, W. Braunschweig et al., Z. Phys. C **47**, 187 (1990); OPAL Collaboration, M. Z. Akrawy et al., Phys. Lett. B **247**, 617 (1990).

[44] CDF Collaboration, D. Acosta et al., Phys. Rev. D **68**, 012003 (2003).

[45] Z.-W. Lin, C. M. Ko, B.-A. Li, B. Zhang, and S. Pal, Phys. Rev. C **72**, 064901 (2005).

[46] B. Müller, The Physics of the Quark-Gluon Plasma, Lecture Notes in Physics Vol. 225, edited by H. Araki, J. Ehlers, K. Hepp, R. Kippenhahn, H. A. Weidenmüller, and J. Zittartz (Springer-Verlag, Berlin, 1985).

[47] PHENIX Collaboration, S. S. Adler et al., Phys. Rev. C **69**, 034910 (2004).